RESEARCH ARTICLE

The ketone body β-Hydroxybutyrate mediated epigenetic chromatin β-hydroxybutyrylation protects kidneys

Juthika Mandal[1,2, *], Sachin Aryal[1,2, *], Ishan Manandhar[1,2, *], Saroj Chakraborty[1,2], Xue Mei[1,2], Beng San Yeoh[1,2], Blair Mell[1,2], Andrew Kleinhenz[3], Ramakumar Tummala[1,2], Tao Yang[1,2], Piu Saha[1,2], William T Gunning III[1,3], Matam Vijay-Kumar[1,2], Venkatesha Basrur[5], Ivana de la Serna[4], Bina Joe[1,2 #]

[1]Center for Hypertension & Precision Medicine; [2]Department of Physiology and Pharmacology; [3]Department of Pathology, [4]Department of Cell and Cancer Biology, University of Toledo College of Medicine and Life Sciences, Toledo, Ohio, USA.

[5]Department of Pathology, Proteomics Resource Facility, University of Michigan, Ann Arbor, Michigan, USA.

---

*Co-First Authors

#Corresponding Author

Bina Joe, PhD, FAHA, FAPS, ISHF

Department of Physiology and Pharmacology

Center for Hypertension and Personalized Medicine

University of Toledo College of Medicine and Life Sciences

312 | Block Health Science Bldg.| 3000 Arlington Ave |Toledo, OH 43614, USA

P: 419.383.4144| bina.joe@utoledo.edu| http://www.utoledo.edu/med/depts/physpharm/

Summary

Starvation, intermittent fasting and exercise, all of which are recommended lifestyle modifiers share a common metabolic signature, ketogenesis to generate the ketone bodies, predominantly β-hydroxybutyrate. β-hydroxybutyrate exerts beneficial effects across various contexts, preventing or mitigating disease. We hypothesized that these dynamic health benefits of β-hydroxybutyrate might stem from its ability to regulate genome architecture through chromatin remodeling via histone β-hydroxybutyrylation, thereby influencing the transcriptome. Focusing on the kidney, which is an end organ protected by β-hydroxybutyrate, we examined histone β-hydroxybutyrylation-mediated chromatin remodeling. Notably, regions of the genome associated with lipid catabolism were predominantly in an open chromatin configuration, leading to active transcription and translation. Significant β-hydroxybutyrylation was observed in the kidneys and the most highly upregulated gene actively transcribed and translated was 3-hydroxy-3-methyglutaryl CoA Synthase 2 (*Hmgcs2*), a gene responsible for the biosynthesis of β-hydroxybutyrate in mitochondria. In contrast, regions with more compact chromatin structures were enriched with genes related to immune function such as protein tyrosine phosphatase receptor type C (*Ptprc*) and lymphocyte cytosolic protein 1 (*Lcp1*), which exhibited reduced transcription and translation. These results reveal that renal epigenetic histone β-hydroxybutyrylation, which concurrently modulates both energy metabolism and immune function is a mechanism underlying the dynamic health effects of β-hydroxybutyrate to protect kidneys and lower hypertension.

Key Words: Blood pressure, histone, energy metabolism, immune function, ketone body, epigenetics, chromatin remodeling

Introduction

β-hydroxybutyrate is a ketone body produced in the liver during the breakdown of fatty acids, especially during periods of low carbohydrate intake, fasting, or prolonged exercise[1]. It is a crucial alternate energy substrate which makes β-hydroxybutyrate essential during states of ketosis, where the body shifts from using carbohydrates to using fats for energy[1,2]. β-hydroxybutyrate is not only a fuel; it also functions as a signaling molecule that can influence gene expression[2]. It modulates pathways related to energy metabolism, inflammation, and oxidative stress[3–5]. β-hydroxybutyrate has been shown to inhibit histone deacetylases, which affect gene transcription, potentially promoting longevity and reducing inflammation[4,6,7]. Particularly related to inflammation, β-hydroxybutyrate is reported to downregulate the expression of the NLRP3 inflammasome[7–9]. It also has antioxidant properties, whereby cells treated with β-hydroxybutyrate are protected from oxidative damage, which is associated with aging and various diseases[10–12]. Due to all these properties, β-hydroxybutyrate confers a beneficial effect on aging as an agent mitigating cellular senescence.

In recent years, there is a growing interest in leveraging β-hydroxybutyrate to help manage chronic metabolic diseases, such as type 2 diabetes, obesity, and cardiovascular diseases[3,9,11,13–15]. We previously examined the effect of β-hydroxybutyrate on blood pressure and discovered that it has a profound antihypertensive effect, which was associated with a betterment of renal function[9]. Reconstitution of β-hydroxybutyrate by oral delivery of its precursor, 1,3 butanediol, preserved renal function and lowered blood pressure in Dahl Salt-Sensitive rats (S), an experimental rat model of hypertension[9].

However, the molecular mechanism by which β-hydroxybutyrate protects kidneys and contributes to lowering of hypertension is not known.

Our study here was designed to examine two known mechanisms regulated by β-hydroxybutyrate. First, we examined whether the beneficial effect of β-hydroxybutyrate was due to inhibition of the NLRP3 inflammasome and secondly, whether it was due to epigenetic β-hydroxybutyrylation mediated chromatin remodeling of the renal transcriptome and proteome. Data in support of the latter as the underlying mechanism are presented.

Results

Targeted disruption of the Nlrp3 inflammasome did not lower blood pressure

In our previous study of the protective effect of β-hydroxybutyrate in a hypertensive rat model with renal disease, we reported downregulation of the Nlrp3 inflammasome[9]. Since β-hydroxybutyrate is known to downregulate Nlrp3, we examined if the absence of Nlrp3 would lower blood pressure. Nlrp3 was targeted and edited in the hypertensive S rat using CRISPR/Cas9 technology. The resultant Nlrp3 knockout rat in the genetic background of S rat had a 14bp deletion in exon 1 which translated into a truncated protein sequence (Figure 1A). The systolic, diastolic, and mean arterial blood pressures of the Nlrp3 knockout were not different from that of the control hypertensive S rat (Figure 1B) indicating that the antihypertensive effect of β-hydroxybutyrate is likely not mediated by Nlrp3.

Enhanced Histone β-hydroxybutyrylation in 1,3-butanediol treated rats

Oral administration of 1,3-butanediol to male rats increased their circulating β-hydroxybutyrate[9]. Here we examined whether the ability of 1,3-butanediol to reconstitute serum β-hydroxybutyrate was sex-independent. As seen in Figure 2A, B, both male and female rats responded to 1,3-butanediol treatment by raising their circulating β-hydroxybutyrate indicating that the conversion of 1,3-butanediol to β-hydroxybutyrate occurred independent of sex.

Next, we investigated if β-hydroxybutyrate resulted in β-hydroxybutyrylation in both male and female rats. As seen in Figures 2C and 2D, both in males as well as in females treated with 1,3-butanediol, there was a significant increase in renal histone 3 lysine-9 β-hydroxybutyrylation. Quantification of data from Figures 2C and 2D are presented in Figures 2E and 2F, which indicate that β-hydroxybutyrylation was more prominent in males than in females. Therefore, for all subsequent studies, male rats were used. Henceforth, this group of male rats with increased renal histone 3 lysine 9 β-hydroxybutyrylation will be referred to as the BHB group.

Histone β-hydroxybutyrylation promoted large-scale chromatin remodeling

To assess the extent of differential chromatin accessibility attributed to histone β-hydroxybutyrylation, we performed ATAC-sequencing. In the BHB group, 3583 genomic regions were detected in the open configuration implying enhanced accessibility for transcriptional regulation (Figure 3A). Similarly, 7728 loci were ‘open’ in the control group indicating that in the BHB group these regions were ‘closed’ or compacted regions of the genome with decreased accessibility for transcription (Figure 3A). Figure 3B shows the proportions of loci in various locations of the genome. Most of the remodeling occurred in the interCGI regions (regions of the genome that lie between CpG islands) followed by

intergenic regions (parts of the genome that lie between genes) and introns. Interestingly, 249 and 196 promoter regions were open in the BHB and control groups respectively (Figure 3B).

Histone β-hydroxybutyrylation-mediated remodeling of the renal transcriptome and proteome

To uncover the extent to which histone β-hydroxybutyrylation regulated the transcriptome, we performed renal RNA-sequencing. In the BHB group compared to the control, a total of 186 genes were upregulated, and 490 genes were downregulated (Figures 3C and 3D). Pathway analysis revealed that the top two upregulated pathways were pantothenate and CoA biosynthesis and fatty acid degradation (Figure 3E).

Next, to examine the impact of the chromatin-remodeling responsive transcriptome on the proteome, we conducted a mass spectrometry-based quantitative proteomic analysis. A volcano plot of the differential proteome is shown in Figure 3F. A total of 119 and 79 proteins were significantly upregulated and downregulated, respectively, in the BHB group compared to control (Figure 3G). Pathway analysis of the proteomics data indicated that butanoate metabolism, fatty acid biosynthesis, and fatty acid metabolism (Figure 3H) were the upregulated whereas pathways downregulated in the BHB group were all related to immune function (Supplementary Figure 1A and Figure 1B).

Chromatin remodeling by histone β-hydroxybutyrylation upregulated lipid catabolism

Next, we explored if the observed alterations in the transcriptome and proteome of the BHB group was specifically due to chromatin remodeling via histone β-

hydroxybutyrylation. To address this, we viewed for shared differentially regulated outputs between chromatin states identified by ATAC-Seq, RNA-seq, and proteomics dataset. Such a combinatorial analysis revealed that there were only 10 upregulated proteins aligned with enhanced transcription caused by histone β-hydroxybutyrylation (Figure 3I). Intriguingly, four of the top genes share a common function, lipid metabolism. These were 3-Hydroxy-3-methylglutaryl-Coenzyme A synthase 2 (*Hmgcs2*), Acetyl-Coenzyme A acetyltransferase 1B (*Acca1b*), Cytochrome P450, family 2, subfamily d, polypeptide 4 (*Cyp2d4*), Cytochrome P450, family 2, subfamily e, polypeptide 1 (*Cyp2e1*) (Figure 3I). Chromatin accessibility of the promoter regions of *Hmgcs2, Acaa1b, Cyp2d4,* and *Cyp2e1* were higher in the BHB group compared to control (Figure 3J). These data indicated that histone β-hydroxybutyration caused chromatin unwinding of the promoter regions of *Hmgcs2, Acaa1b, Cyp2d4,* and *Cyp2e1.* Reactome pathway analysis using the 10 genes identified metabolism as the top upregulated pathway along with several other pathways such as metabolism of lipids, synthesis and metabolism of ketone bodies, and β-oxidation of very long chain fatty acids (Figure 3I).

Collectively, these results provide a basis to further prioritize and validate β-hydroxybutyrylation as a key mechanism underlying the preference of S rats to utilize lipids as their primary source for energy.

Metabolic reprogramming in response to elevated histone β-hydroxybutyrylation

To determine if the histone β-hydroxybutyrylation-mediated changes in gene and protein expression resulted in increased transcription of key genes in lipid catabolism, resulted in increased fatty acid oxidation, we housed both control and BHB group of rats in the Comprehensive Lab Animal Monitor System (CLAMS) and monitored their metabolic

parameters. Overall, both oxygen consumption (VO_2) and carbon dioxide production (VCO_2) were lower in the BHB group compared to control (Figure 4A and 4B). Importantly, respiratory exchange ratio (RER) was dramatically decreased in the BHB group compared to the control group (Figure 4C). A lower RER points to lipids, but not carbohydrates as the primary source of energy. These data provided further evidence that histone β-hydroxybutyrylation enhanced transcription of key metabolic genes in the lipid mobilizing pathways. Those key genes, *Hmgcs2, Acaa1b, Cyp2d4 and Cyp2e*1 contributed to a preferential switch in bioenergetic fuel source to lipids instead of glucose (Figure 4C).

Hmgcs2, _Acaa1b_, _Cyp2d4_, and _Cyp2e1_ are bonafide targets linking epigenetic renal Histone-3 β-hydroxybutyrylation to energy metabolism

In addition to β-hydroxybutyrylation, β-hydroxybutyrate is also known to epigenetically modify histones by acetylation[7,16]. Therefore, it was important to determine whether the 4 upregulated energy metabolism genes, *Hmgcs2*, *Acaa1b*, *Cyp2d4*, and *Cyp2e1*, which were prioritized in our study were specific targets of β-hydroxybutyration. To do so, we performed Chromatin immunoprecipitation (ChIP) assays using an antibody specific to β-hydroxybutyryl-histone H3 (Lys 9) β-hydroxybutyrate. ChIP assay using this antibody revealed that promoter regions of *Hmgcs2*, *Acaa1b*, *Cyp2d4*, and *Cyp2e1* were significantly enriched in the BHB group (Figure 5A), thus confirming that these genes were bonafide targets of β-hydroxybutyrylation.

Next, transcripts of these genes were quantitated by real time qPCR analysis. The abundance of Hmgcs2 was prominently upregulated by ~15 fold higher in the BHB group compared to control (Figure 5B, Supplementary Figure 2A). Similarly, the abundances of

Acaa1b, *Cyp2d4* and *Cyp2e1* were also upregulated, *albeit* to lower extents of 3-4-fold in the BHB group compared to controls (Figure 5B, Supplementary Figure 2B-2D). Aligned with these data, quantitative mass-spectrometry using high-quality MS3 spectra indicated that all 4 protein products of *Hmgcs2*, *Acaa1b*, *Cyp2d4* and *Cyp2e1* were significantly upregulated in the BHB group compared to control (Figure 5C). Taken together, these data demonstrate that β-hydroxybutyrate, via conferring epigenetic histone β-hydroxybutyrylation upregulated proteins which mobilize lipids for energy metabolism.

Upregulation of Hmgcs2-mediated fatty acid oxidation increased renal proximal tubule epithelial cell mitochondrial circulatory index

One of the prominent targets upregulated due to histone β-hydroxybutyrylation was the mitochondrial protein Hmgcs2. Hmgcs2 is a cytosolic and rate-limiting enzyme regulating mitochondrial fatty acid oxidation to promote ketogenesis. Ketogenesis is largely attributed to the liver, but recent work demonstrates that Hmgcs2 in the kidneys also participates in this pathway[17,18]. Because ketogenesis in the liver causes alterations in shape of mitochondria, predominantly circular form, we asked if such alterations in the ultrastructure of mitochondria also occur in the kidney. Transmission electron microscopy revealed more circular mitochondria in the proximal tubule epithelial cells from the BHB group compared to the elongated mitochondria in the controls (Figure 6A). This observation was confirmed by morphometric analyses of the measurement of average mitochondrial area, area/perimeter, and circularity index of these mitochondria. As seen in Figures 6B, 6C and 6D, each of these morphometric measures were elevated in the BHB supplemented group compared to the controls. These data support our conclusion

that histone β-hydroxybutyrylation mediated upregulation of Hmgcs2 to promote ketosis contributed to enhanced renal mitochondrial circularity index.

Upregulation of Acaa1b-mediated fatty acid oxidation increased peroxisomal biogenesis

Fatty acid oxidation occurs both in mitochondria and peroxisomes[19–21]. Whereas mitochondria are the main site of oxidation of medium-and long-chain fatty acids, peroxisomes catalyze the β-oxidation of a distinct set of fatty acids, including very-long-chain fatty acids[22–24]. While Hmgcs2 is located within mitochondria, interestingly, another target of histone β-hydroxybutyrylation, acetyl-Coenzyme A acyltransferase 1B (Acaa1b), which is responsible for β-oxidation of fatty acids, is located within peroxisomes[25,26]. In response to metabolic stress, peroxisomes proliferate by upregulating their biogenesis[27]. One of the factors required for peroxisomal biogenesis is peroxisomal biogenesis factor 11 γ[28]. Interestingly, proteomic data revealed that Pex11γ was increased in the BHB group, which indicated that peroxisomal biogenesis was promoted in the BHB group (Supplementary Figure 3A). To further confirm this observation, we examined the renal sections for the abundance of peroxisomes using the classical marker, peroxisomal membrane protein 70 (Pmp70). Peroxisome staining was more prominent in the BHB group compared to control (Supplementary Figure 3B and 3C). Therefore, we concluded that the upregulation of Acaa1b, the peroxisomal target of histone-β-hydroxybutyrylation, placed an increased demand for fatty acid oxidation, which in turn resulted in increased peroxisome biogenesis.

β-hydroxybutyrylation-mediated enhanced fatty acid oxidation inhibits Mammalian Target of Rapamycin Complex 1 (mTORC1).

Stimulation of peroxisome biogenesis by drugs such as rapamycin are known to inhibit mammalian target of rapamycin complex 1 (mTORC1) activity[29,30]. Hyperactivation of mTORC1 signaling is associated with a variety of human diseases whereas suppression of mTORC1 is known to curb senescence, extend lifespan of yeast, *C. elegans*, *Drosophila* and mice and promote autophagy[31]. Importantly, mTORC1 inhibits fatty acid β-oxidation, whereas inhibition of mTORC1 by rapamycin promotes fatty acid oxidation[32]. Importantly, rapamycin suppresses mTORC1 signaling to ameliorate kidney injury and hypertension in S rats[33]. Based on the similarity in function between rapamycin and the targets of β-hydroxybutyrylation to promote fatty acid oxidation, we hypothesized that mTORC1 is inhibited in the BHB group to protect kidneys. In support, mTORC1 was significantly inhibited in the BHB group compared to control (Figure 4D, 4E, Supplementary Figure 4A and 4B).

Chromatin remodeling by histone β-hydroxybutyrylation resulted in downregulation of immune function genes

Next, we examined the downregulated loci, transcripts and proteins in the BHB group compared to control. Similar to the shared upregulated genes and proteins, the combinatorial analysis using ATAC-seq, transcriptomic, and proteomic datasets showed that only 9 proteins were downregulated in all the 3 analyses (Figure 7A). Among these, the top 2 were protein tyrosine phosphatase receptor type C (*Ptprc*) and Lymphocyte cytosolic protein 1 (*Lcp1*). Chromatin accessibility of the promoter regions of *Ptprc* and *Lcp1* were lower in the BHB group compared to control (Figure 7B and Figure 7C). These results indicate that histone β-hydroxybutyrylation mediated chromatin compaction of the promoter regions of *Ptprc* and *Lcp1* contributed to the observed lower transcription

(Figure 7D, 7E and Supplementary Figure 5A, 5B) and translation (Figure 7F and 7G) of these loci.

Unlike the upregulated pathways of energy metabolism, reactome pathway analysis of the downregulated genes showed that the overall downregulated pathways due to histone β-hydroxybutyration were related to immune function. These were phosphorylation of CD3 and TCR zeta chains, downstream TCR signaling, translocation of ZAP-70 to immunological synapse, PD-1 signaling, immune system, interferon gamma signaling, interleukin-12 family signaling, and TCR signaling (Figure 7A).

Histone β-hydroxybutyration promoted downregulation of CD45 and LCP-1

Next, we focused on the two top genes which were prominently downregulated in our ATAC-seq study, *Ptprc* and *Lcp-1*. Lower expression of both *Ptprc* and *Lcp1* in the BHB group was confirmed by qPCR (Figure 7D and 7E). These data correlated with lower abundance of the protein products of these genes (CD45 and LCP-1, respectively) in the BHB group compared to the controls (Figure 7H and 7I). CD45 and LCP-1 are both important for the function of T cells and dysfunctional regulation of T cells are implicated in renal disease and hypertension. Therefore, we focused on examining T cells using $CD3^+$ as a pan marker reporting for all T cells in our experimental groups.

Lower expression of CD45 and LCP-1 enhanced $CD3^+$ T cells proliferation

Both CD45 and LCP-1 are present in all hematopoietic cells[34–37]. Therefore, we examined if the downregulation of these two genes in the BHB group was facilitated by the epigenetic action of β-hydroxybutyrate reflected in immunomodulatory effects. Analysis of complete blood count (CBC) revealed a significant decrease in the level of circulating

white blood cells (WBCs), specifically lymphocytes, in the BHB group (Figure 7H and 7I). Similarly, mean corpuscular volume, mean corpuscular hemoglobin, mean platelet volume, plateletcrit, platelet distribution width was also lower in the BHB group. These data affirm an immunomodulatory function of β-hydroxybutyrate (Figure 7A, Supplementary Figure 6A-6F). In alignment with this observation, the parent population of CD3+ T cells was lower in the BHB group compared to controls (Figure 7J). Intriguingly, CD3+ T cells from the BHB group exhibited increased proliferation as indicated by a higher population of dividing cells (D2) while maintaining a similar population of D1 populations (Figure 7J and 7K). These findings suggest that lower expression of CD45 and LCP-1 in the BHB group contributed to a rapid turnover of T lymphocytes by depleting existing parental cells and promoting the generation of a sufficient number of new effector T cells, thus contributing to an enhanced immune response to combat inflammation and maintain immune homeostasis.

Discussion

In this study, we sought to examine the molecular mechanism underlying the protective effect of β-hydroxybutyrate[9]. Because BHB inhibits Nlrp3, first we generated a novel targeted CRISPR mediated Nlrp3-gene edited hypertensive rat, we examined its blood pressure and report that disruption of the *Nlrp3* locus did not lower blood pressure. This ruled out the possibility of Nlrp3 as the mediator for the observed beneficial effect of β-hydroxybutyrate. Next, we examined the known function of β-hydroxybutyrate to epigenetically remodel chromatin by histone β-hydroxybutyrylation[38]. Chromatin remodeling by histone β-hydroxybutyrylation exerted dynamic effects of distinctly modifying the renal transcriptome and proteome to promote both mitochondrial and

peroxisomal regulation of fatty acid catabolism while parallelly dampening immune cell function. Our work here has methodically dissected and characterized the major loci, transcripts and proteins contributing to the specific and dynamic consequence of renal histone β-hydroxybutyrylation to conclude that epigenetic chromatin remodeling by histone β-hydroxybutyrylation simultaneously regulates the dual processes of upregulation of fatty acid catabolism and dampening of immune cells. These results constitute a new mechanism underlying the dynamic beneficial renoprotective effect of β-hydroxybutyrate.

Histone β-hydroxybutyrylation was first identified as a new epigenetic modification occurring in the mouse liver in response to starvation[38], which is a condition simultaneously promoting ketosis and anti-senescence pathways. Being a ketone body and well recognized as an anti-senescent molecule, β-hydroxybutyrate is central to both pathways promoted by starvation[11,39,40]. Its epigenetic action to post translationally modify histones by β-hydroxybutyrylation has been subsequently studied in the context of a variety of pathologies including cardiomyopathy[41], depression[42], glomerulosclerosis[43], and lung adenocarcinoma[44], but not in any renal or hemodynamic studies. While our previous study on the benefit of β-hydroxybutyrate[9] has been reproduced by others in different contexts such as preeclampsia and diabetic kidney disease, the underlying molecular mechanism has remained elusive[45–47]. In this context, our results presented in this study are the first to reveal that post translational modification of histones by β-hydroxybutyration is a novel mechanism protecting the kidneys.

Pathway analysis revealed an upregulation of fatty acid metabolism. Mitochondria, a major organelle involved in fat metabolism, undergoes changes in morphology based on

nutrient availability and stress conditions. mTORC1 is a known regulator of numerous cellular processes, such as cell proliferation, metabolism, and cell growth[48]. mTORC1 regulates mitochondrial metabolism and controls mitochondrial biogenesis[49]. Mitochondrial fission and apoptosis are controlled by mechanistic/mammalian target of rapamycin complex 1 (mTORC1) mediated stimulated translation of mitochondrial fission process 1 (MTFP1)[50]. Our study showed a distinct mitochondrial morphological alteration occurring in response to β-hydroxybutyrate, whereby mitochondria were more circular. Reduced circularity of mitochondria is reported to increase fatty acid oxidation, which concur with our findings[51]. Further, our data demonstrate that increased fatty acid oxidation was linked to a significant inhibition of mTORC1. In support, rapamycin, which is a uniquely specific mTOR inhibitor, increases fatty acid oxidation[32]. Similarly, fenofibrate, which is reported to have beneficial cardiovascular and renal effects, increased fatty acid oxidation and inhibited mTOR[52]. Importantly, in the context of salt-sensitive hypertension and kidney injury, Kumar *et al*. (2017), have shown the inhibition of mammalian target of rapamycin 1 (mTORC1) ameliorates both hypertension and renal injury[49]. These data taken together with our findings reported in the current study leads us to propose that epigenetic chromatin remodeling by histone β-hydroxybutyration promotes the renal fatty acid oxidation-mTORC1 axis to protect kidneys and lower hypertension.

An interesting finding of our study is that Hmgcs2, which is the main enzyme catalyzing the production of β-hydroxybutyrate from Acetyl CoA, is also the target locus impacted by β-hydroxybutyration. This indicates that β-hydroxybutyrate autoregulates its own production by epigenetically remodeling chromatin to promote the transcription of

Hmgcs2. If this process is perpetual, systemic β-hydroxybutyrate levels would remain consistently elevated after a single intervention to raise systemic β-hydroxybutyrate. Such a dysregulated continuous production of β-hydroxybutyrate would be detrimental as it would lead to ketoacidosis. Besides, β-hydroxybutyrate is elevated only during fasting and is lowered during the fed state[9]. Similarly, β-hydroxybutyrylation was discovered to be elevated only during fasting[38]. Collectively, these data lend support to the notion that histone β-hydroxybutyrylation by β-hydroxybutyryrate is not perpetual but turned 'off' when β-hydroxybutyryrate is limiting and/or by yet undiscovered mechanisms.

A very low-carbohydrate diet is reported to enhance human T-cell immunity through immunometabolic reprogramming[53]. Such a low carbohydrate diet could promote ketosis and inhibit mTOR. mTOR inhibition by Rapamycin, which also lowers hypertension, is shown to promote T cell hypo responsiveness or anergy[49]. In alignment with these observations, the downregulated pathways generated from downregulated genes/proteins led to lowering of T cell signaling, which implies that the mechanism by which T cell signaling is affected by β-hydroxybutyrate is a result of epigenetic remodeling of chromatin to a condensed state in regions harboring *Ptprc* and *Lcp1*.

Conclusion

This is a comprehensive study furthering our understanding that renal epigenetic histone β-hydroxybutyrylation is a fundamental new mechanism by which β-hydroxybutyrate serves as a beneficial metabolite for preserving renal function and lowering hypertension. Specifically, our results reveal that histone β-hydroxybutyrylation causes a dynamic increase in chromatin accessibility to the promoter regions harboring lipid catabolizing genes while simultaneously decreasing accessibility to the promoter regions of genes

contributing to immune-related functions. Together, these newly discovered mechanisms underly the beneficial effects of β-hydroxybutyrate on renal-hemodynamic health.

Author Contributions

BJ designed the study, JM, SC, SA, IM, MX, BSY, BM, AK, RT, PS, WTG, VB, IDLS collected and analyzed data; JM, SC, MX, BSY, BM, AK, RT, PS, WTG, VB, IDLS, SA, IM, MVK interpreted the data, SA, IM, BJ, JM, SC, VB, WTG, IDLS, PS contributed to writing the manuscript, All authors read and edited the manuscript. All authors provided their permission for the submission and publication of this manuscript. It has not been accepted or published elsewhere.

Declaration of Interests

None.

Funding

Support for this work from the National Heart, Lung and Blood Institute of the National Institutes of Health to BJ is gratefully acknowledged (R01-HL171401-01). Predoctoral fellowship from the American Heart Association to SA (25PRE1375711) and IM (24PRE1186688). Funding support from the Crohn's and Colitis Foundation and American Heart Association Career Development Award to PS (854385 and 855256, respectively). Liver Scholar Award from the American Liver Foundation to BSY. University of Toledo Startup funds and the American Heart Association Career Development Award (852969) to TY. Funding support from the National Institutes of Health to MVK

(R01DK134053). Support from Melanoma Research Foundation (MRF) and University of Toledo Stimulus and Bridge Awards to IDS.

Supplemental Information Titles and Legends

Document S1. Figures S1-S5

Figure Legends

Figure 1: *Nlrp3* is not linked to lowering of hypertension. (A) Genotyping data of the founder $S^{Nlrp3-/-}$ rats. (B.) Systolic blood pressure of male S (n=5) and SS-*Nlrp3*^{em2} (n=5) rats; All data are mean±SEM; not significant between groups. *Nlrp3*: NOD-like receptor protein 3, WT: Wild-type.

Figure 2: Histone β-hydroxybutyrylation is elevated with 1,3-butanediol treatment. (A-B) Serum levels of β-hydroxybutyrate in males and females. (C-D) Immunoblotting for β-hydroxybutyrylation. (E-F) Quantification of the blots. BHB: β-hydroxybutyrate, H3K9BHB: Histone 3 lysine 9 β-hydroxybutyrylation, H3: Histone 3. All data are mean ±SEM, *p<0.05, **p<0.01.

Figure 3: Chromatin accessibility, gene expression, and protein levels are altered with 1,3-butanediol treatment. (A) Volcano plot for BHB vs. control groups. Each data point is a tested locus. The vertical lines correspond to the logFC cutoff. (B) Annotation summary of loci tested in BHB vs control groups. X-axis: genomic annotations; Y-axis proportion of loci in each category within each type of annotation. All Tested Loci (red bars), serve as a basis by which to compare the significant loci (blue and green bars). (C) RNAseq data: Volcano plot representing the significantly differential transcripts. The X-axis: log2 normalized fold change in BHB group compared to control; The Y-axis: –log10 of adjusted p value. (D) Differentially expressed transcripts in numbers. The black bar indicates upregulated transcripts, and the gray bar indicates downregulated transcripts in the BHB group compared to the control. (E) Pathways associated with the upregulated genes of BHB group. (F) Proteomics data: Volcano plot depicting significantly altered

protein levels. X-axis: log2 normalized fold change in the BHB group compared to control. Y-axis: –log10 of adjusted p value. (G) Differentially expressed proteins in numbers. The black bar indicates upregulated proteins, and the grey bar indicates downregulated proteins in BHB groups compared to the control. (H) Pathways associated with upregulated proteins in the BHB group. (I) Venn diagram showing common upregulated genes and corresponding proteins leading to increased metabolism. Different shades of blue circles depict ATACseq, RNAseq, and Proteomics data and numbers within the circles are numbers of genes/proteins significantly upregulated. The gray box provides the name for common upregulated genes and proteins; Underneath are the associated upregulated pathways. (J) Chromatin accessibility for genes of interest. The y-axis represents chromatin cut sites and thus open chromatin, and x-axis represents the chromatin location of genes of interest. Black peaks represent the control group, and green peaks represent BHB group.

Figure 4: 1,3-butanediol treatment reduces respiratory exchange ratio (RER) and inhibits mammalian target of rapamycin complex 1 (mTORC1). (A-C) Metabolic CLAMS data showed reduced VO_2, VCO_2, and RER level in the BHB group compared to controls. Black line: control group and green line: BHB group. (D-E) Reduced phospho-S6 ribosomal protein levels were found in male rats treated with BHB compared to control. See also Supplementary Figure S4 for data from female rats. BHB: β-hydroxybutyrate. All data are mean±SEM; *$p \leq 0.05$, **$p \leq 0.01$, and ***$p \leq 0.001$.

Figure 5: Validation of common upregulated genes through CHIP-qPCR, Real time PCR, and proteomics. (A) CHIP-qPCR data demonstrating enrichment of *Hmgcs2, Acaa1b, Cyp2d4,* and *Cyp2e1* in the BHB group compared to control (n=3

replicates/group). Black bar: Control, Green bar: BHB. (B) Real time PCR showed higher expression of *Hmgcs2*, *Acaa1b*, *Cyp2d4*, and *Cyp2e1* in BHB group compared to control (housekeeping gene is *L36a*). (C) Normalized relative abundance of Hmgcs2, Acaa1b, Cyp2d4, Cyp2e1 proteins. See also Supplementary Figure S2 for female data. Black open circle- control, green closed circle- BHB. All data are mean±SEM; *p< 0.05, **p< 0.01, ***p< 0.001, ****p <0.0001 and #p=0.0567.

Figure 6: Kidney proximal tubule epithelial cell mitochondrial circulatory index was found to be higher in BHB group compared to control. (A) Representative transmission electron microscopy images of renal mitochondria. Orange arrows point to mitochondria. (B-D) Bar graph shows quantification (B) Average mitochondrial area (C) Area/Perimeter, and (D) Circularity index. BHB: β-hydroxybutyrate. n=30 images per group. All data are mean±SEM, ***p< 0.001, and ****p<0.0001.

Figure 7: Chromatin accessibility, gene expression, protein levels, and $CD3^+$ T cells proliferation were altered with 1,3-butanediol treatment. (A) Venn diagrams showing common downregulated genes and proteins leading to downregulation of immune function pathways. Different shades of blue circles are used to indicate ATACseq, RNAseq, and Proteomics data. The gray box lists the names of common downregulated genes and proteins, beneath which are shown the associated downregulated pathways. (B) Chromatin accessibility at the promoter region of *Ptprc* and (C) Chromatin accessibility at the *Lcp1* promoter. The y-axis represents chromatin cut sites and thus open chromatin, and x-axis represents the chromatin location of genes of interest. Black peaks represent the control group, and green peaks represent BHB group. (D-E) Real time PCR data showing reduced expression with *Ptprc* and *Lcp1* in the 1,3-butanediol supplementation.

(F-G) Normalized relative abundances of Ptprc (Cd45) and Lcp1 detected in the quantitative proteomics study. Black open circle– control, green closed circle- BHB. (H-I) Complete blood count (H) Peripheral white blood cells and (I) Lymphocytes in the control and BHB treated male S rats. (J) Representative histogram for percent CFSE-positive CD3+ T cells. (K) Quantification for percent CFSE-positive $CD3^+$ T cells in control and BHB groups after 5 days. Data represented as Mean ± SEM and N was plotted for control and BHB group. WBC: white blood cells, Lym: Lymphocytes, CFSE: carboxyfluorescein diacetate succinimidyl ester, CD3: Cluster of differentiation 3, P= Parent population, D1= Daughter 1, and D2= Daughter 2 population All data are mean±SEM, *p<0.05, **p< 0.01, ***p< 0.001 and ****p<0.0001.

Supplementary Figure 1: BHB supplementation downregulates pathway related to immune cell function. (A) Pathways regulated by downregulated genes within the BHB group, (B) Pathways regulated by downregulated proteins in BHB group.

Supplementary Figure 2: Validation of common upregulated and downregulated genes in female rat kidney. (A-D) Real time PCR data depicting significant upregulation of *Hmgcs2, Acaa1b*, *Cyp2d4* in the BHB supplemented female rats. (E-F) *Ptprc* and *Lcp1* showed downregulated trend in the BHB treated group compared to the control. Housekeeping gene: β-actin. All data are mean±SEM, *p< 0.05 and ***p< 0.001. ns: Data trending but not significant.

Supplementary Figure 3: Lower protein cast and higher peroxisome in rats treated with BHB. (A) Proteomics data depicting upregulation of Pex11γ level in BHB

supplemented male rat kidney. Data are mean± SEM, *p< 0.05. (B-C) Representative images (8x and 40x magnifications) of kidney sections with immunostaining for peroxisomes (Pmp70, brown color); (B) control S rats and (C) 1,3-butanediol fed rats. Relatively higher intensity of brown color was observed in the BHB group compared to control. IHC-PMP: Immunohistochemistry-peroxisomal membrane protein.

Supplementary Figure 4: BHB inhibits MTORC1 activity in the BHB supplemented female kidney. (A-B) Reduced phospho-S6/S6 ribosomal protein in female kidneys from the BHB group compared to controls. Data are mean ±SEM, *p< 0.05.

Supplementary Figure 5: Chromatin Immunoprecipitation assay, food intake and activity in male rats. (A) Comparable Chromatin immunoprecipitation data from kidneys of male rats for *Ptprc* and *Lcp1* promoters with H3K9 β-hydroxybutyrylated histones. (n=3 replicates/group) (B) Significantly lower 24-hour food intake in the BHB group. (n=5/group) (C) No differences in 24-hour average activity between BHB and control groups. All data are mean ± SEM; Ns: p>0.05, ***p< 0.001.

Supplemental Figure 6: BHB restores blood parameters as indicated by the complete blood count. (A) Mean corpuscular volume (MCV). (B) Mean corpuscular hemoglobin (MCH). (C) Mean platelet volume (MPV). (D) Plateletcrit (PCT). (E-F) Platelet distribution width (PDW). Data represented as Mean ± SEM. *p<0.05, **p<0.01, ***p<0.0001.

Star Methods

Key Resources Table

REAGENT or RESOURCE	SOURCE	IDENTIFIER
Antibodies		
Anti-β-hydroxybutyryl-Histone H3 (Lys9) rabbit pAb	PTM Bio	Cat# PTM-1250
Anti-Histone H3 rabbit pAB (CT)	PTM Bio	Cat# PTM-1002
Rabbit IgG	Millipore Sigma	
Phospho-S6 Ribosomal Protein (Ser235/236) Rabbit mAb	Cell Signaling Technology	Cat# 4858
S6 Ribosomal Protein Rabbit mAb	Cell Signaling Technology	Cat# 2217
Chemicals, Peptides and Recombinant Proteins		
(±)-1,3-Butanediol	Sigma-Aldrich	Cat# B84785
Trizol reagent	Invitrogen	Cat# 15596-026
RIPA Lysis buffer	Thermofisher Scientific	Cat#89900
Critical Commercial Assays		

β-Hydroxybutyrate Colorimetric Assay kit	Cayman Chemicals	Cat# 700190
Deposited Data		
Experimental Models: Organisms/ Strains		
Dahl Salt sensitive rats/ S	University of Toledo	https://rgd.mcw.edu/rgdweb/report/strain/main.html?id=69369
SS-*Nlrp3*^{em2}rat	Medical College of Wisconsin	MCW Gene Editing Rat Resource Center
Oligonucleotides		
See Supplementary Tables 1 and 2 for primer sequences	Current manuscript	N/A
Software and Algorithms		
GraphPad Prism 10.1.0	GraphPad software	https://www.graphpad.com/
ShinyGO 0.77	South Dakota State University	http://bioinformatics.sdstate.edu/go/
Reactome v86	Reactome	https://reactome.org/
SnapGene 7.0	Dotmatics	https://www.snapgene.com/
ImageJ	National Institute of Health	https://imagej.net/ij/

Quantstudio Design & Analysis	Thermo Scientific	https://apps.thermofisher.com/apps/da2/#/home/
Microsoft 365	Microsoft	https://www.office.com/
Reagents and Resources		
Harlan Teklad low salt diet	Envigo	Cat#TD7034
Harlan Teklad high salt diet	Envigo	Cat#TD94217
Radiotelemetry transmitters	Data Science Int.	PA-C10
SpectraMax M3	Molecular Devices	N/A
Nanodrop 2000	Thermo Scientific	N/A
VS120 Virtual Slide Microscope	Olympus	N/A
Talos L120C G2 3D Tomography Transmission Electron Microscope	ThermoFisher Scientific	N/A
Covaris CryoPREP2	Covaris	N/A
NovaSeq6000 Sequencing system	Illumina	N/A

Contact for Reagents and Resource Sharing.

Further requests for any information and reagents should be directed to the lead contact Dr. Bina Joe (bina.joe@utoledo.edu).

Experimental Models and Subject Details

SS$^{Nlrp3-/-}$aka (SS-*Nlrp3*$^{em2)}$ rat was obtained from the Medical College of Wisconsin (MCW Gene Editing Rat Resource Center). Inbred S male and female rats maintained at the University of Toledo College of Medicine were used. All breeding and experimental procedures were performed in accordance with the Guide for the Care and Use of Laboratory Animals and were reviewed and approved by the Institutional Animal Care and Use Committee of the University of Toledo College of Medicine and Life Sciences. Pups were weaned between 28-30 days. All rats were maintained on a 12:12 h light-dark cycle and were allowed free access to chow, unless specifically fasted overnight; water was always provided *ad libitum*. Rats were raised on a 0.3% NaCl containing diet (Harlan Teklad diet TD 7034, Madison, WI) until 40 days of age when they were switched to a 2% NaCl containing diet (Harlan Teklad diet TD94217, Madison, WI) and randomly assigned to two experimental groups administered with or without 20% (v/v) of stock 1, 3-butanediol in their drinking water for 5-weeks. Female rats were less tolerant to the dose as indicated by >20% loss of body weight, whereby on the third week, 1, 3- Butanediol was lowered to (10% v/v). After 5 weeks of 1, 3- butanediol treatment, rats were euthanized by thoracotomy and exsanguination via cardiac puncture under isoflurane anesthesia administered via a nose cone (5% in 100% O_2). This was consistent with the American Veterinary Medical Association Guidelines for the Euthanasia of Animals. All euthanasia and tissue harvesting were performed in the University of Toledo Department of Laboratory Animal Resources. Serum and kidneys were collected and stored at -80ºC.

Methods

Blood Pressure and Activity Measurement

Radiotelemetry transmitters were surgically implanted in rats as described previously[54]. Rats were closely monitored after surgery and allowed to recover for 4 days before blood pressure (BP) measurements were obtained using the Data Sciences International (DSI) software and equipment (https://www.datasci.com/). Systolic, diastolic, mean arterial pressure (MAP) and activity were collected at 5-minute intervals and BP data and activity was analyzed using the Dataquest A.R.T 4.2 Software.

Monitoring Energy Metabolism

Metabolic parameters were measured in 12 to13-week old male rats after 8 weeks of 1,3-BD supplementation. Comprehensive Laboratory Animal Monitoring System (CLAMS, Columbus Instruments), an integrated open-circuit calorimeter, was used for measuring whole-body metabolic states for 24 hours following the manufacturer's instructions. Briefly, oxygen consumption (VO_2) and carbon dioxide production (VCO_2) in each chamber were sampled sequentially for 5 seconds in a 10-minute interval and motor activity was recorded every second in X and Z dimensions. Respiratory exchange ratio (RER) was calculated as VCO_2/VO_2.

Food Intake

Rats were housed individually and given 100-120 grams of food, which were measured and documented in metabolic cages. After 24 hours, the left-over food was weighed, and the difference was recorded as food intake.

Measurement of Serum BHB

While the rats were under isoflurane anesthesia, but prior to thoracotomy and exsanguination by cardiac puncture, arterial blood was collected from the abdominal aorta

in silicone-coated collection tubes specifically used for serum collection (BD Vacutainer). Blood was set aside to clot at room temperature for ~20 min, centrifuged at 2000 g for 15 min at 4°C and the serum collected was flash frozen in liquid nitrogen, and stored at -80°C. Thawed serum was used to quantitate BHB using a colorimetric assay kit from Cayman Chemicals. Briefly, sera were diluted 1:5 using the assay buffer provided. Standards and samples were incubated with the developer solution at 25°C in the dark and optical density was measured at 450 nm using a SpectraMax M3 microplate reader from Molecular Devices (Sunnyvale, CA, USA).

Histone Extraction

Snap-frozen kidney samples were homogenized using a Dounce homogenizer (50 strokes) in ice-cold pre-lysis buffer. Histones were extracted using the EpiQuik total histone extraction kit and quantitated using the BCA (Bicinchoninic Acid) method[55]. Proteins were aliquoted and stored at -80ºC until further use for gel electrophoresis on a 4-20% gradient SDS PAGE gel.

Western Blotting

Histones were probed using primary antibodies obtained from PTM Biolabs (www.ptmbiolabs.com). Antibodies used in the study are mentioned in the Key Resource Table.

ATAC-Sequencing

Library preparation: Flash frozen renal tissues were transported to the UM Epigenomics Core for ATAC-Seq library preparation. Briefly, the tissues were cryo-pulverized with a Covaris CryoPREP2 (Covaris,). Frozen tissue powder (100mg) was aliquoted and

processed for isolation of nuclei, enriched using an Optiprep discontinuous gradient and tagmented according to the Omni-ATAC-Seq protocol[56]. The concentration of nuclei was assessed and a total of 50,000 nuclei were used for tagmentation. The final libraries were cleaned using Qiagen MinElute columns and AMPure XP beads before quantitation with the Qubit HS dsDNA kit, and quality assessment on a TapeStation HS D1000 kit. The libraries were pooled and quantitated by qPCR using KAPA's Illumina Library quantitation kit before PE-150 sequencing on a NovaSeq6000 S4 at the University of Michigan advanced Genomics Core.

Pipeline: Data preprocessing and quality controlling were performed using the bioinformatics pipeline, snakemake[57]. FastQC (FastQC) (v0.11.8) was used for Quality control of raw reads and trimmed reads[58]. TrimGalore (TrimGalore) (v0.4.5) and cutadapt (Martin) (v1.15) were used for adapter trimming and filtering of low-quality bases. Trimmed reads were aligned to rn6 with Bowtie2[59]. Alignment quality control was performed using samtools[60]. Reads completely overlapping blacklisted regions (ENCODE Blacklist Regions) were removed with bedtools[61]. Sample-wise peaks were called with macs2[62]. Peaks over all samples were merged with bedops[63] for principal component analysis and unsupervised clustering to assess the similarity of samples. Finally, a report was generated by MultiQC[64]. For ATAC specific QC metrics, ataqv (Ataqv) was used[65].

Differential Peaks:

For each model and contrast, the edgeR R Bioconductor package[66] (v3.28.1) was used to identify regions of differentially open chromatin (DOC). For each sample, the number of reads in the merged peaks is counted for each sample, and a library size normalization

factor was determined. With no replicates, the BCV (biological coefficient of variance) parameter was tuned. Each model was then fitted using the glmFit function, and each contrast was tested with a likelihood ratio test and for the replicates, the common, trended, and tagwise negative binomial dispersions were calculated. Each model was then fitted using the glmQLFit function, and each contrast was tested with an empirical Bayes quasi-likelihood F-test. The DOC were then annotated to genic and CpG island annotations using the annotatr Bioconductor package (v1.12.1)[67]. The threshold used to determine DOC was false discovery rate (FDR) < 0.05 and fold change (FC) >1.

RNA Extraction and Real Time PCR Analysis

Total RNA was extracted from control and 1, 3-Butanediol fed rat kidneys using Trizol (Invitrogen). RNA was reverse transcribed to cDNA using SuperScript III kit (Invitrogen). Levels of mRNA expression of *Acaa1b*, *Hmgcs2*, *Cyp2d4*, *Cyp2e1*, *Ptprc* and *Lcp1* (primer sequence shown in Table S2) were analyzed by real-time PCR (Applied Biosystems), and expression levels relative to the expression of *B-Actin* and *L36a* were calculated by the $2^{-\Delta\Delta Ct}$ method[68].

RNA Sequencing

RNA extracted with the Trizol method was assessed for RNA quantity and purity with a Bioanalyzer 2100 and RNA 6000 Nano LabChip Kit (Agilent, CA, USA, 5067-1511) and dispatched to LC Sciences (Houston, TX). RNA with RIN number > 7.0 were considered of high quality and used to construct sequencing library. Two rounds of mRNA purification were conducted from total RNA (5ug) using Dynabeads Oligo (dT) (Thermo Fisher, CA, USA). Following purification, the mRNA was fragmented into short fragments using divalent cations under elevated temperature (Magnesium RNA Fragmentation Module

(NEB, cat.e6150, USA) under 94℃ 5-7min). Next, the cleaved RNA fragments were reverse transcribed to create the cDNA by SuperScript™ II Reverse Transcriptase (Invitrogen, cat. 1896649, USA), which were then used to synthesize U-labeled second-stranded DNAs with E. coli DNA polymerase I (NEB, cat.m0209, USA), RNase H (NEB, cat.m0297, USA) and dUTP Solution (Thermo Fisher, cat.R0133, USA). An A-base was then added to the blunt ends of each strand, preparing them for ligation to the indexed adapters. Each adapter contained a T-base overhang for ligating the adapter to the A-tailed fragmented DNA. Dual-index adapters were ligated to the fragments, and size selection was performed with AMPureXP beads. After the heat-labile UDG enzyme (NEB, cat.m0280, USA) treatment of the U-labeled second-stranded DNAs, the ligated products were amplified with PCR by the following conditions: initial denaturation at 95℃ for 3 min; 8 cycles of denaturation at 98℃ for 15 sec, annealing at 60℃ for 15 sec, and extension at 72℃ for 30 sec; and then final extension at 72℃ for 5 min. The average insert size for the final cDNA librarys were 300±50 bp. At last, we performed the 2×150bp paired-end sequencing (PE150) on an Illumina Novaseq™ 6000 following the vendor's recommended protocol. The sequence quality was verified using FastQC (http://www.bioinformatics.babraham.ac.uk/projects/fastqc/, 0.11.9) [69,70].

Quantitative Proteomic Analysis by Mass-spectrometry

Kidneys were lysed using RIPA Lysis and Extraction buffer according to the manufacturer's instructions. Proteins were quantified using the BCA assay, diluted to. 2mg/ml and shipped to the University of Michigan Proteomics Resource Facility for proteomic analysis. The protocol for Tandem Mass Tag labeling and offline fractionation was followed as described in Cheng et al., 2020[71]. Briefly, the TMT 6plex kit (#90061)

was used for TMT labeling according to the manufacturer's protocol (ThermoFisher Scientific). 100 ug protein was taken from each respective groups and DTT was used for the reduction reaction and alkylation with 2 chloroacetamide was done after that. Precipitation of proteins was done using ice-cold acetone and overnight incubation at -20 °C. Precipitated protein pellet was resuspended in Triethylammonium bicarbonate (TEAB) and overnight digestion was carried out using trypsin. (Promega, V5113). Digested peptides were transferred to TMT reagents reconstituted by anhydrous acetonitrile. Hydroxylamine was added and incubated. All samples were combined and dried. Prior to MS analysis, high pH reverse phase fractionation was performed, and fractions were dried and reconstituted in loading buffer containing 0.1% formic acid and 2% acetonitrile. Liquid Chromatography-mass spectrometry analysis (LC-Multinotch MS3) was performed followed by using Proteome Discoverer (v2.1; Thermo Fisher) for data analysis. Identified proteins and peptides were filtered to retain only those that passed ≤1% FDR threshold. Quantitation was performed using high-quality MS3 spectra (Average signal-to-noise ratio of 10, less than 30% isolation inference, and data was normalized against total peptide).

ChIP Assay

Rat tissue was ground to a fine powder with a mortar and pestle then crosslinked with 1% formaldehyde and homogenized as in[72,73]. Nuclei were isolated[74] in Lysis Buffer 1 (50mM HEPES-KOH, pH 7.5, 140mM NaCl, 1mM EDTA, 10% glycerol, 0.5% NP40, 0.25% TritonX, and protease inhibitors) then washed with Lysis Buffer 2 (10mM Tris-HCl, pH 8.0, 200mM NaCl, 1mM EDTA, 0.5mM EGTA and protease inhibitors). Nuclei were re-suspended in Lysis Buffer 3 (10mM Tris-HCl, pH 8.0. 100mM NaCl, 9mM EDTA, 0.5mM

EGTA, 0.1% Na-Deoxycholate, and 0.5% N-lauryolsarcosine, protease inhibitors) and sonicated in 30 second pulses at 60% power, for a total of 6 minutes to get an average fragment size of 200-1000 base pairs. A small portion (1%) of the chromatin was saved as “Input”. Approximately 25µg of chromatin was pre-cleared for one hour at 4°C with Protein A Sepharose (Cytiva, Marlborough, MA, USA), then incubated overnight with an antibody to β-hydroxybutyryl-histone H3 (Lys 9) (H3K9BHB) (PTM Biolabs, Chicago, Il, USA) or normal rabbit IgG (Millipore Sigma, St. Louis, MO, USA) in Lysis Buffer 3, supplemented with 1.1% Triton X-100. Protein A sepharose was added the next morning and incubation was allowed to proceed for an additional four hours. The precipitated chromatin was then washed five times in RIPA buffer (50 mM HEPES, 500 mM LiCl, 0.1 mM EDTA, 1.0% NP-40 and 0.7% Na-Deoxycholate) and once with TE containing 50mM NaCl. Complexes were then eluted with 50 mM Tris [pH 8.0], 10 mM EDTA and 1.0% SDS. Crosslinks were reversed by overnight incubation at 65^{0}C. After proteinase K digestion, DNA was purified by phenol/chloroform extraction and ethanol precipitation. Genomic regions of interest were identified from ATAC-seq data, and the sequences retrieved using the UCSC Genome Browser. Primers were designed using the Primer 3.0 tool version 4.1.0[75,76]. PCR amplifications were performed on an ABI 7500 system (Thermo Fisher, Waltham, MA, USA) using SYBR green master mix (Qiagen, Hilden, Germany). Data were analyzed using ABI 7500 software to generate cycle thresholds (CT values). Delta CT values were calculated by subtracting the CT values of the ChIPs obtained with the antibodies of interest from the CT values of the Input controls. The $2^{-\Delta\Delta Ct}$ method was then used to calculate enrichment of immunoprecipitated material. Average ChIP enrichment was calculated from three biological replicates, each amplified

as three technical replicates. Primer sequences for ChIPs PCR are mentioned in supplemental table 2.

Pathway Analyses

The KEGG based pathway enrichment analyses was conducted on upregulated genes and proteins using ShinyGOv0.77 (FDR cut off <0.05)[77]. From the common up and downregulated genes, Reactome pathway knowledgebase was used to generate pathways[78].

Transmission Electron Microscopy and Analysis of Mitochondrial Morphology

Fresh minced or formalin fixed tissues (not frozen) were placed into sodium cacodylate buffered with 3% glutaraldehyde (pH 7.4) at room temperature for 1 1/2 - 2 hours. Specimens were gently agitated throughout the tissue processing procedure. Samples were subsequently washed with 2-3 changes of fresh cacodylate buffer (pH 7.4) for a total time of 20-30 minutes, then immersed in cold (4ºC) 1% osmium tetroxide (OsO4) in cacodylate buffer (pH 7.4) for 1 1/2 - 2 hours at room temperature. Following OsO4 fixation 2-3 changes of fresh cacodylate buffer were used for washing for a total of 20-30 minutes. Tertiary fixation was included using an aqueous saturated solution of uranyl acetate in distilled water (pH 3.3) for 1.0 hour. The tissues were dehydrated at room temperature with an increasing concentration of ethanol (50%, 70%, 90%, 95%, and 100%) followed by 100% acetone. Samples were then infiltrated with a 50% acetone**:** 50% embedding media (Araldite 502/Embed 812) overnight at room temperature. The next day, tissues were embedded in appropriately labeled embedding capsules filled with fresh 100% Araldite 502/Embed 812 embedding media. Capsules were polymerized in a 65ºC oven overnight. A Leica Reichert Ultracut S

Ultramicrotome (Austria) was used to obtain 75-80 nm thin sections that were collected upon 300 mesh copper grids and post-section stained with uranyl acetate and Reynolds lead citrate and examined using a Talos L120C G2 3D Tomography Transmission Electron Microscope (ThermoFisher Scientific, USA). Images were obtained at 6700X magnification to provide a minimum of 1000 mitochondria per group for image analysis to calculate average mitochondrial area, perimeter and mitochondrial circularity index using ImageJ software from NIH.

Quantification of peripheral T cells proliferation

Blood samples were collected in EDTA tubes from control and BHB treated male S rats and peripheral lymphocytes were isolated via Histopaque method. Briefly, lymphocytes ($1x10^6$ cells/well) were stained with carboxyfluorescein diacetate succinimidyl ester (CFSE, Sigma, 5 µM) and washed, then cultured in 1% heat inactivated fetal bovine serum (HI-FBS) in DMEM media for 5 days. Then, cells were washed and stained with anti-rat CD3-APC antibody in staining buffer (PBS+ 1% FBS) for 40 min, cells were washed and acquired via flow cytometer (BD AccuriTM C6 Plus).

Histological Analyses

Kidneys were fixed in neutral buffered formalin after the sacrifice and after 24 hours it was transferred to 70% ethanol for paraffin-embedding and sectioning via microtome. To observe the morphological and histopathological changes kidney sections were stained with Hematoxylin & eosin. Paraffin embedded kidney sections were de-paraffinized and immersed in citrate buffer for epitope retrieval. After blocking with horse serum, the sections were incubated overnight with rabbit anti-PMP70 antibody (ThermoFisher

Scientific, Cat# PA1-650, 1:100 dilution). PMP70 was detected by using Vectastain Elite ABC kit and SigmaFast 3,3-Diamino-benzidine tablets. The images were visualized and captured by using VS120 Virtual Slide Microscope (Olympus). The images were analyzed by Olyvia Ver.2.9 software.

Quantification and Statistical Analyses

GraphPad Prism version 9.3.1 was used for data analysis. Statistical analyses were performed using the student's t-test to compare between two groups and one-way ANOVA with Bonferroni post hoc test for > 2 group comparisons. Data with a p-value < 0.05 was considered significant. All bar graph values were presented as Mean ± SEM.

Supplemental Table 1: Primers for Real Time q-PCR

Gene	**Sequence (5'-3')** (Forward & Reverse Primers)
Hmgcs2	CGGAGACGCATGTCCCCTGA
	AATGGTTGTATGGATTGGCCTCCTT
Ptprc	ACCTGCTCGCACCACTGAAT
	GCAGAGGGGGTCTGTGAGTC
Cyp2e1	CCTGCATGGCTACAAGGCTG
	GGGAAAACCTCCGCACATCC
Cyp2d4	ATGATGAGAACCTGCGTGTGG
	TCGATTTCCTGTTGTACTCGGC
Acaa1b	CTTCTGTCGGCCGTGTTGAC
	GGCCCCGGGCTGAAG
Lcp1	AGGGATCTGTGCGATCGGTG
	TCGGGTTCATGGGGATGACG
L36a	ATTGTGCTCAGGCTTGAGTGT
	TGG ATCACTTGACCCTTT

Supplemental Table 2: Primers for ChIP PCR

Gene	**Sequence (5'-3')** (Forward & Reverse Primers)
Hmgcs2	ACCTTTGGCCCAGTTTTTCT
	GGTGAGAGCGAAGATTCCTG
Ptprc	AAGCCCTCCTGTGTCCAATA
	GTGCACATGTGTAGGGGTGT
Cyp2e1	TAAAGGCTCCAAGGTTCAGC
	GAGAAGGAGGGTGGCTCATC
Cyp2d4	GGGAGAGGTGAAGGAGGAGA
	GGATCTGCCTCCTCAGAGTG
Acaa1b	CCTAGCATCGATGTGTGCAG
	AGAGCCCAAAACTCGAAAGG
Lcp1	CAGAAAGGCCAAGGAGTCAG
	CCACCAATAACGGAGATGCT

1. Wang, L., Chen, P., and Xiao, W. (2021). β-hydroxybutyrate as an Anti-Aging Metabolite. Nutrients *13*, 3420.

2. Newman, J.C., and Verdin, E. (2017). β-Hydroxybutyrate: a signaling metabolite. Annu. Rev. Nutr. *37*, 51–76.

3. Huang, C., Wang, J., Liu, H., Huang, R., Yan, X., Song, M., Tan, G., and Zhi, F. (2022). Ketone body β-hydroxybutyrate ameliorates colitis by promoting M2 macrophage polarization through the STAT6-dependent signaling pathway. BMC Med. *20*, 148.

4. Shimazu, T., Hirschey, M.D., Newman, J., He, W., Shirakawa, K., Le Moan, N., Grueter, C.A., Lim, H., Saunders, L.R., and Stevens, R.D. (2013). Suppression of oxidative stress by β-hydroxybutyrate, an endogenous histone deacetylase inhibitor. Science (80-.). *339*, 211–214.

5. Hwang, C.Y., Choe, W., Yoon, K.-S., Ha, J., Kim, S.S., Yeo, E.-J., and Kang, I. (2022). Molecular mechanisms for ketone body metabolism, signaling functions, and therapeutic potential in cancer. Nutrients *14*, 4932.

6. Edwards, C., Canfield, J., Copes, N., Rehan, M., Lipps, D., and Bradshaw, P.C. (2014). D-beta-hydroxybutyrate extends lifespan in C. elegans. Aging (Albany NY) *6*, 621.

7. Deng, Y., Xie, M., Li, Q., Xu, X., Ou, W., Zhang, Y., Xiao, H., Yu, H., Zheng, Y., and Liang, Y. (2021). Targeting mitochondria-inflammation circuit by β-hydroxybutyrate mitigates HFpEF. Circ. Res. *128*, 232–245.

8. Youm, Y.-H., Nguyen, K.Y., Grant, R.W., Goldberg, E.L., Bodogai, M., Kim, D., D'agostino, D., Planavsky, N., Lupfer, C., and Kanneganti, T.D. (2015). The ketone metabolite β-hydroxybutyrate blocks NLRP3 inflammasome–mediated inflammatory disease. Nat. Med. *21*, 263–269.

9. Chakraborty, S., Galla, S., Cheng, X., Yeo, J.-Y., Mell, B., Singh, V., Yeoh, B., Saha, P., Mathew, A. V, and Vijay-Kumar, M. (2018). Salt-responsive metabolite, β-hydroxybutyrate, attenuates hypertension. Cell Rep. *25*, 677–689.

10. Qiao, G., Lv, T., Zhang, M., Chen, P., Sun, Q., Zhang, J., and Li, Q. (2020). β-hydroxybutyrate (β-HB) exerts anti-inflammatory and antioxidant effects in lipopolysaccharide (LPS)-stimulated macrophages in Liza haematocheila. Fish Shellfish Immunol. *107*, 444–451.

11. Fang, Y., Chen, B., Gong, A.Y., Malhotra, D.K., Gupta, R., Dworkin, L.D., and Gong, R. (2021). The ketone body β-hydroxybutyrate mitigates the senescence response of glomerular podocytes to diabetic insults. Kidney Int. *100*, 1037–1053.

12. Kovács, Z., Brunner, B., and Ari, C. (2021). Beneficial effects of exogenous ketogenic supplements on aging processes and age-related neurodegenerative diseases. Nutrients *13*, 2197.

13. McCarthy, C.G., Chakraborty, S., Singh, G., San Yeoh, B., Schreckenberger, Z.J., Singh, A., Mell, B., Bearss, N.R., Yang, T., and Cheng, X. (2021). Ketone body β-hydroxybutyrate is an autophagy-dependent vasodilator. JCI insight *6*.

14. Ortí, J.E. de la R., Cuerda-Ballester, M., Sanchis-Sanchis, C.E., Lajara Romance, J.M., Navarro-Illana, E., and García Pardo, M.P. (2023). Exploring the impact of

ketogenic diet on multiple sclerosis: obesity, anxiety, depression, and the glutamate system. Front. Nutr. *10*, 1227431.

15. Hanners, A., Melnyk, B.M., Volek, J., and Kelley, M.M. (2022). Ketogenic diet, African American women, and cardiovascular health: A systematic review. Worldviews Evidence-Based Nurs. *19*, 35–41.

16. He, Y., Cheng, X., Zhou, T., Li, D., Peng, J., Xu, Y., and Huang, W. (2023). β-Hydroxybutyrate as an epigenetic modifier: Underlying mechanisms and implications. Heliyon.

17. Feola, K., Venable, A.H., Broomfield, T., Villegas, M., Fu, X., Burgess, S., and Huen, S.C. (2024). Hepatic ketogenesis is not required for starvation adaptation in mice. Mol. Metab. *86*, 101967.

18. Venable, A.H., Lee, L.E., Feola, K., Santoyo, J., Broomfield, T., and Huen, S.C. (2022). Fasting-induced HMGCS2 expression in the kidney does not contribute to circulating ketones. Am. J. Physiol. Physiol. *322*, F460–F467.

19. Mi, Y., Qi, G., Vitali, F., Shang, Y., Raikes, A.C., Wang, T., Jin, Y., Brinton, R.D., Gu, H., and Yin, F. (2023). Loss of fatty acid degradation by astrocytic mitochondria triggers neuroinflammation and neurodegeneration. Nat. Metab. *5*, 445–465.

20. Talari, N.K., Mattam, U., Meher, N.K., Paripati, A.K., Mahadev, K., Krishnamoorthy, T., and Sepuri, N.B. V (2023). Lipid-droplet associated mitochondria promote fatty-acid oxidation through a distinct bioenergetic pattern in male Wistar rats. Nat. Commun. *14*, 766.

21. Liu, S., Zhang, H., Li, Y., Zhang, Y., Bian, Y., Zeng, Y., Yao, X., Wan, J., Chen, X., and Li, J. (2021). S100A4 enhances protumor macrophage polarization by control of PPAR-γ-dependent induction of fatty acid oxidation. J. Immunother. cancer *9*.

22. Panov, A. V, Mayorov, V.I., Dikalova, A.E., and Dikalov, S.I. (2022). Long-chain and medium-chain fatty acids in energy metabolism of murine kidney mitochondria. Int. J. Mol. Sci. *24*, 379.

23. Cappa, M., Todisco, T., and Bizzarri, C. (2023). X-linked adrenoleukodystrophy and primary adrenal insufficiency. Front. Endocrinol. (Lausanne). *14*, 1309053.

24. Chevillard, G., Clémencet, M.-C., Latruffe, N., and Nicolas-Francès, V. (2004). Targeted disruption of the peroxisomal thiolase B gene in mouse: a new model to study disorders related to peroxisomal lipid metabolism. Biochimie *86*, 849–856.

25. Bai, M., Wu, M., Jiang, M., He, J., Deng, X., Xu, S., Fan, J., Miao, M., Wang, T., and Li, Y. (2023). LONP1 targets HMGCS2 to protect mitochondrial function and attenuate chronic kidney disease. EMBO Mol. Med. *15*, e16581.

26. Liu, C., Fu, C., Lu, Y., Sun, J., Liu, T., Wang, Y., Wang, A., Huang, Y., and Li, Y. (2024). Integration of metabolomics and transcriptomics to reveal the mechanism of Gerberae piloselloidis herba in alleviating bronchial asthma. J. Ethnopharmacol. *325*, 117852.

27. Lodhi, I.J., and Semenkovich, C.F. (2014). Peroxisomes: a nexus for lipid metabolism and cellular signaling. Cell Metab. *19*, 380–392.

28. Li, X., and Gould, S.J. (2002). PEX11 promotes peroxisome division independently of peroxisome metabolism. J. Cell Biol. *156*, 643–651.

29. Dunlop, E.A., and Tee, A.R. (2009). Mammalian target of rapamycin complex 1: signalling inputs, substrates and feedback mechanisms. Cell. Signal. *21*, 827–835.

30. Eun, S.Y., Lee, J.N., Nam, I.-K., Liu, Z., So, H.-S., Choe, S.-K., and Park, R. (2018). PEX5 regulates autophagy via the mTORC1-TFEB axis during starvation. Exp. Mol. Med. *50*, 1–12.

31. Kucheryavenko, O., Nelson, G., von Zglinicki, T., Korolchuk, V.I., and Carroll, B. (2019). The mTORC1-autophagy pathway is a target for senescent cell elimination. Biogerontology *20*, 331–335.

32. Sipula, I.J., Brown, N.F., and Perdomo, G. (2006). Rapamycin-mediated inhibition of mammalian target of rapamycin in skeletal muscle cells reduces glucose utilization and increases fatty acid oxidation. Metabolism *55*, 1637–1644.

33. Kumar, V., Evans, L.C., Kurth, T., Yang, C., Wollner, C., Nasci, V., Zheleznova, N.N., Bukowy, J., Dayton, A., and Cowley Jr, A.W. (2019). Therapeutic suppression of mTOR (mammalian target of rapamycin) signaling prevents and reverses salt-induced hypertension and kidney injury in Dahl salt-sensitive rats. Hypertension *73*, 630–639.

34. Hermiston, M.L., Xu, Z., and Weiss, A. (2003). CD45: a critical regulator of signaling thresholds in immune cells. Annu. Rev. Immunol. *21*, 107–137.

35. Rheinländer, A., Schraven, B., and Bommhardt, U. (2018). CD45 in human physiology and clinical medicine. Immunol. Lett. *196*, 22–32.

36. Kell, M.J., Riccio, R.E., Baumgartner, E.A., Compton, Z.J., Pecorin, P.J., Mitchell, T.A., Topczewski, J., and LeClair, E.E. (2018). Targeted deletion of the zebrafish actin-bundling protein L-plastin (lcp1). PLoS One *13*, e0190353.

37. Wabnitz, G., Balta, E., and Samstag, Y. (2017). L-plastin regulates the stability of the immune synapse of naive and effector T-cells. Adv. Biol. Regul. *63*, 107–114.

38. Xie, Z., Zhang, D., Chung, D., Tang, Z., Huang, H., Dai, L., Qi, S., Li, J., Colak, G., and Chen, Y. (2016). Metabolic regulation of gene expression by histone lysine β-hydroxybutyrylation. Mol. Cell *62*, 194–206.

39. Han, Y., Bedarida, T., Ding, Y., Somba, B.K., Lu, Q., Wang, Q., Song, P., and Zou, M.-H. (2018). β-Hydroxybutyrate prevents vascular senescence through hnRNP A1-mediated upregulation of Oct4. Mol. Cell *71*, 1064–1078.

40. Xia, G., Wen, Z., Zhang, L., Huang, J., Wang, X., Liang, C., Cui, X., Cao, X., and Wu, S. (2023). β-Hydroxybutyrate alleviates cartilage senescence through hnRNP A1-mediated up-regulation of PTEN. Exp. Gerontol. *175*, 112140.

41. Luo, W., He, M., Luo, Q., and Li, Y. (2023). Proteome-wide analysis of lysine β-hydroxybutyrylation in the myocardium of diabetic rat model with cardiomyopathy. Front. Cardiovasc. Med. *9*, 1066822.

42. Chen, L., Miao, Z., and Xu, X. (2017). β-hydroxybutyrate alleviates depressive behaviors in mice possibly by increasing the histone3-lysine9-β-

hydroxybutyrylation. Biochem. Biophys. Res. Commun. *490*, 117–122.

43. Luo, W., Yu, Y., Wang, H., Liu, K., Wang, Y., Huang, M., Xuan, C., Li, Y., and Qi, J. (2020). Up-regulation of MMP-2 by histone H3K9 β-hydroxybutyrylation to antagonize glomerulosclerosis in diabetic rat. Acta Diabetol. *57*, 1501–1509.

44. Huang, J., Liang, L., Jiang, S., Liu, Y., He, H., Sun, X., Li, Y., Xie, L., Tao, Y., and Cong, L. (2023). BDH1-mediated LRRC31 regulation dependent on histone lysine β-hydroxybutyrylation to promote lung adenocarcinoma progression. MedComm *4*, e449.

45. Ishimwe, J.A., Baker, M.B., Garrett, M.R., and Sasser, J.M. (2022). Periconceptional 1, 3-butanediol supplementation suppresses the superimposed preeclampsia-like phenotype in the Dahl salt-sensitive rat. Am. J. Physiol. Circ. Physiol. *322*, H285–H295.

46. Wan, S.-R., Teng, F.-Y., Fan, W., Xu, B.-T., Li, X.-Y., Tan, X.-Z., Guo, M., Gao, C.-L., Zhang, C.-X., and Jiang, Z.-Z. (2023). BDH1-mediated βOHB metabolism ameliorates diabetic kidney disease by activation of NRF2-mediated antioxidative pathway. Aging (Albany NY) *15*, 13384.

47. Kim, M.N., Moon, J.H., and Cho, Y.M. (2021). Sodium-glucose cotransporter-2 inhibition reduces cellular senescence in the diabetic kidney by promoting ketone body-induced NRF2 activation. Diabetes, Obes. Metab. *23*, 2561–2571.

48. Szwed, A., Kim, E., and Jacinto, E. (2021). Regulation and metabolic functions of mTORC1 and mTORC2. Physiol. Rev. *101*, 1371–1426.

49. Kumar, V., Wollner, C., Kurth, T., Bukowy, J.D., and Cowley Jr, A.W. (2017). Inhibition of mammalian target of rapamycin complex 1 attenuates salt-induced hypertension and kidney injury in Dahl salt-sensitive rats. Hypertension *70*, 813–821.

50. Morita, M., Prudent, J., Basu, K., Goyon, V., Katsumura, S., Hulea, L., Pearl, D., Siddiqui, N., Strack, S., and McGuirk, S. (2017). mTOR controls mitochondrial dynamics and cell survival via MTFP1. Mol. Cell *67*, 922–935.

51. Ngo, J., Choi, D.W., Stanley, I.A., Stiles, L., Molina, A.J.A., Chen, P., Lako, A., Sung, I.C.H., Goswami, R., and Kim, M. (2023). Mitochondrial morphology controls fatty acid utilization by changing CPT1 sensitivity to malonyl-CoA. EMBO J. *42*, e111901.

52. Lian, X., Gu, J., Gao, B., Li, Y., Damodaran, C., Wei, W., Fu, Y., and Cai, L. (2018). Fenofibrate inhibits mTOR-p70S6K signaling and simultaneously induces cell death in human prostate cancer cells. Biochem. Biophys. Res. Commun. *496*, 70–75.

53. Hirschberger, S., Strauß, G., Effinger, D., Marstaller, X., Ferstl, A., Müller, M.B., Wu, T., Hübner, M., Rahmel, T., and Mascolo, H. (2021). Very-low-carbohydrate diet enhances human T-cell immunity through immunometabolic reprogramming. EMBO Mol. Med. *13*, e14323.

54. Mell, B., Jala, V.R., Mathew, A. V, Byun, J., Waghulde, H., Zhang, Y., Haribabu, B., Vijay-Kumar, M., Pennathur, S., and Joe, B. (2015). Evidence for a link between gut microbiota and hypertension in the Dahl rat. Physiol. Genomics *47*,

187–197.

55. Walker, J.M. (2009). The bicinchoninic acid (BCA) assay for protein quantitation. protein Protoc. Handb., 11–15.

56. Corces, M.R., Trevino, A.E., Hamilton, E.G., Greenside, P.G., Sinnott-Armstrong, N.A., Vesuna, S., Satpathy, A.T., Rubin, A.J., Montine, K.S., and Wu, B. (2017). An improved ATAC-seq protocol reduces background and enables interrogation of frozen tissues. Nat. Methods *14*, 959–962.

57. Köster, J., and Rahmann, S. (2012). Snakemake—a scalable bioinformatics workflow engine. Bioinformatics *28*, 2520–2522.

58. Ou, J., Liu, H., Yu, J., Kelliher, M.A., Castilla, L.H., Lawson, N.D., and Zhu, L.J. (2018). ATACseqQC: a Bioconductor package for post-alignment quality assessment of ATAC-seq data. BMC Genomics *19*, 1–13.

59. Langmead, B., and Salzberg, S.L. (2012). Fast gapped-read alignment with Bowtie 2. Nat. Methods *9*, 357–359.

60. Li, H., Handsaker, B., Wysoker, A., Fennell, T., Ruan, J., Homer, N., Marth, G., Abecasis, G., and Durbin, R. (2009). The sequence alignment/map format and SAMtools. Bioinformatics *25*, 2078–2079.

61. Quinlan, A.R., and Hall, I.M. (2010). BEDTools: a flexible suite of utilities for comparing genomic features. Bioinformatics *26*, 841–842.

62. Zhang, Y., Liu, T., Meyer, C.A., Eeckhoute, J., Johnson, D.S., Bernstein, B.E., Nusbaum, C., Myers, R.M., Brown, M., and Li, W. (2008). Model-based analysis

of ChIP-Seq (MACS). Genome Biol. *9*, 1–9.

63. Neph, S., Kuehn, M.S., Reynolds, A.P., Haugen, E., Thurman, R.E., Johnson, A.K., Rynes, E., Maurano, M.T., Vierstra, J., and Thomas, S. (2012). BEDOPS: high-performance genomic feature operations. Bioinformatics *28*, 1919–1920.

64. Ewels, P., Magnusson, M., Lundin, S., and Käller, M. (2016). MultiQC: summarize analysis results for multiple tools and samples in a single report. Bioinformatics *32*, 3047–3048.

65. Orchard, P., Kyono, Y., Hensley, J., Kitzman, J.O., and Parker, S.C.J. (2020). Quantification, dynamic visualization, and validation of bias in ATAC-seq data with ataqv. Cell Syst. *10*, 298–306.

66. McCarthy, D.J., Chen, Y., and Smyth, G.K. (2012). Differential expression analysis of multifactor RNA-Seq experiments with respect to biological variation. Nucleic Acids Res. *40*, 4288–4297.

67. Cavalcante, R.G., and Sartor, M.A. (2017). Annotatr: genomic regions in context. Bioinformatics *33*, 2381–2383.

68. Livak, K.J., and Schmittgen, T.D. (2001). Analysis of relative gene expression data using real-time quantitative PCR and the 2− ΔΔCT method. methods *25*, 402–408.

69. Thompson, O., von Meyenn, F., Hewitt, Z., Alexander, J., Wood, A., Weightman, R., Gregory, S., Krueger, F., Andrews, S., and Barbaric, I. (2020). Low rates of mutation in clinical grade human pluripotent stem cells under different culture

conditions. Nat. Commun. *11*, 1528.

70. Martin, M. (2011). Cutadapt removes adapter sequences from high-throughput sequencing reads. EMBnet. J. *17*, 10–12.

71. Cheng, X., Mell, B., Alimadadi, A., Galla, S., McCarthy, C.G., Chakraborty, S., Basrur, V., and Joe, B. (2020). Genetic predisposition for increased red blood cell distribution width is an early risk factor for cardiovascular and renal comorbidities. Dis. Model. Mech. *13*, dmm044081.

72. Mehrotra, A., Joe, B., and de la Serna, I.L. (2013). SWI/SNF chromatin remodeling enzymes are associated with cardiac hypertrophy in a genetic rat model of hypertension. J. Cell. Physiol. *228*, 2337–2342.

73. Perna, A., and Alberi, L.A. (2019). TF-ChIP method for tissue-specific gene targets. Front. Cell. Neurosci. *13*, 95.

74. Basuroy, T., Dreier, M., Baum, C., Blomquist, T., Trumbly, R., Filipp, F. V, and de la Serna, I.L. (2023). Epigenetic and pharmacological control of pigmentation via Bromodomain Protein 9 (BRD9). Pigment Cell Melanoma Res. *36*, 19–32.

75. Untergasser, A., Cutcutache, I., Koressaar, T., Ye, J., Faircloth, B.C., Remm, M., and Rozen, S.G. (2012). Primer3—new capabilities and interfaces. Nucleic Acids Res. *40*, e115–e115.

76. Kõressaar, T., Lepamets, M., Kaplinski, L., Raime, K., Andreson, R., and Remm, M. (2018). Primer3_masker: integrating masking of template sequence with primer design software. Bioinformatics *34*, 1937–1938.

77. Ge, S.X., Jung, D., and ShinyGO, R.Y. A graphical gene-set enrichment tool for animals and plants., 2020, 36. DOI https//doi. org/10.1093/bioinformatics/btz931, 2628–2629.

78. Milacic, M., Beavers, D., Conley, P., Gong, C., Gillespie, M., Griss, J., Haw, R., Jassal, B., Matthews, L., and May, B. (2024). The reactome pathway knowledgebase 2024. Nucleic Acids Res. *52*, D672–D678.

Figure 1

A.

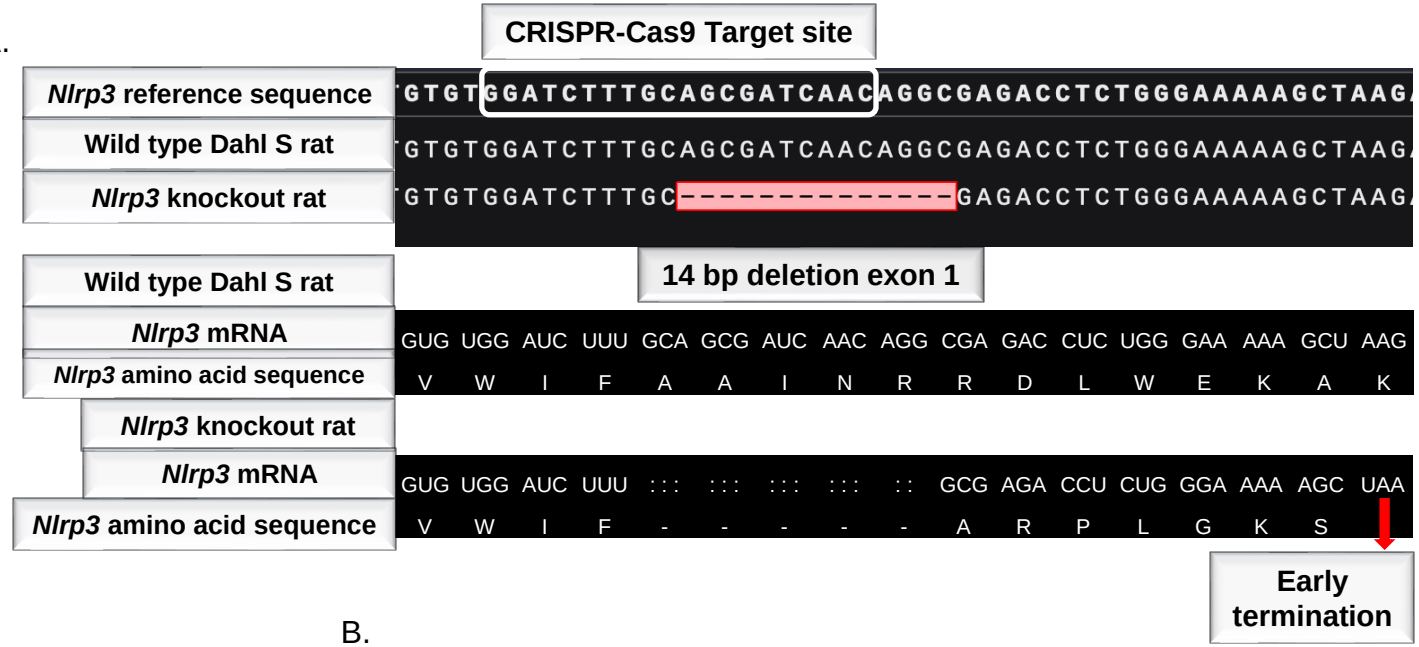
CRISPR-Cas9 Target site
Nlrp3 reference sequence
Wild type Dahl S rat
Nlrp3 knockout rat
GTGTGGATCTTTGCAGCGATCAACAGGCGAGACCTCTGGGAAAAAGCTAAG
GTGTGGATCTTTGC----------GAGACCTCTGGGAAAAAGCTAAG
14 bp deletion exon 1
Wild type Dahl S rat
Nlrp3 mRNA
Nlrp3 amino acid sequence
GUG UGG AUC UUU GCA GCG AUC AAC AGG CGA GAC CUC UGG GAA AAA GCU AAG
V W I F A A I N R R D L W E K A K
Nlrp3 knockout rat
Nlrp3 mRNA
Nlrp3 amino acid sequence
GUG UGG AUC UUU ::: ::: ::: ::: :: GCG AGA CCU CUG GGA AAA AGC UAA
V W I F - - - - - A R P L G K S
Early termination

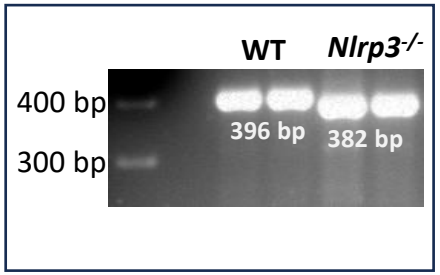
WT
Nlrp3-/-
400 bp
300 bp
396 bp
382 bp

B.

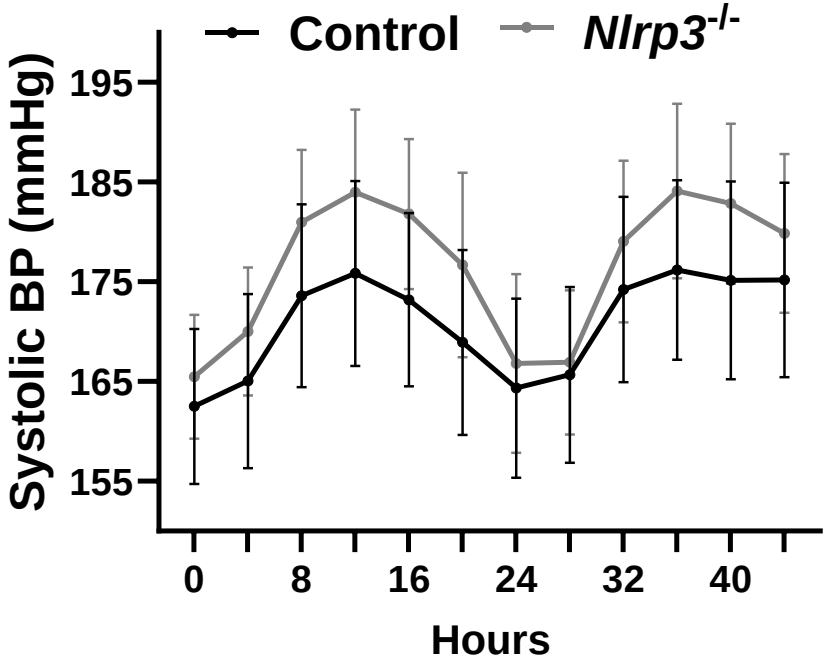
Control
Nlrp3-/-
Systolic BP (mmHg)
195
185
175
165
155
0
8
16
24
32
40
Hours

Figure 2

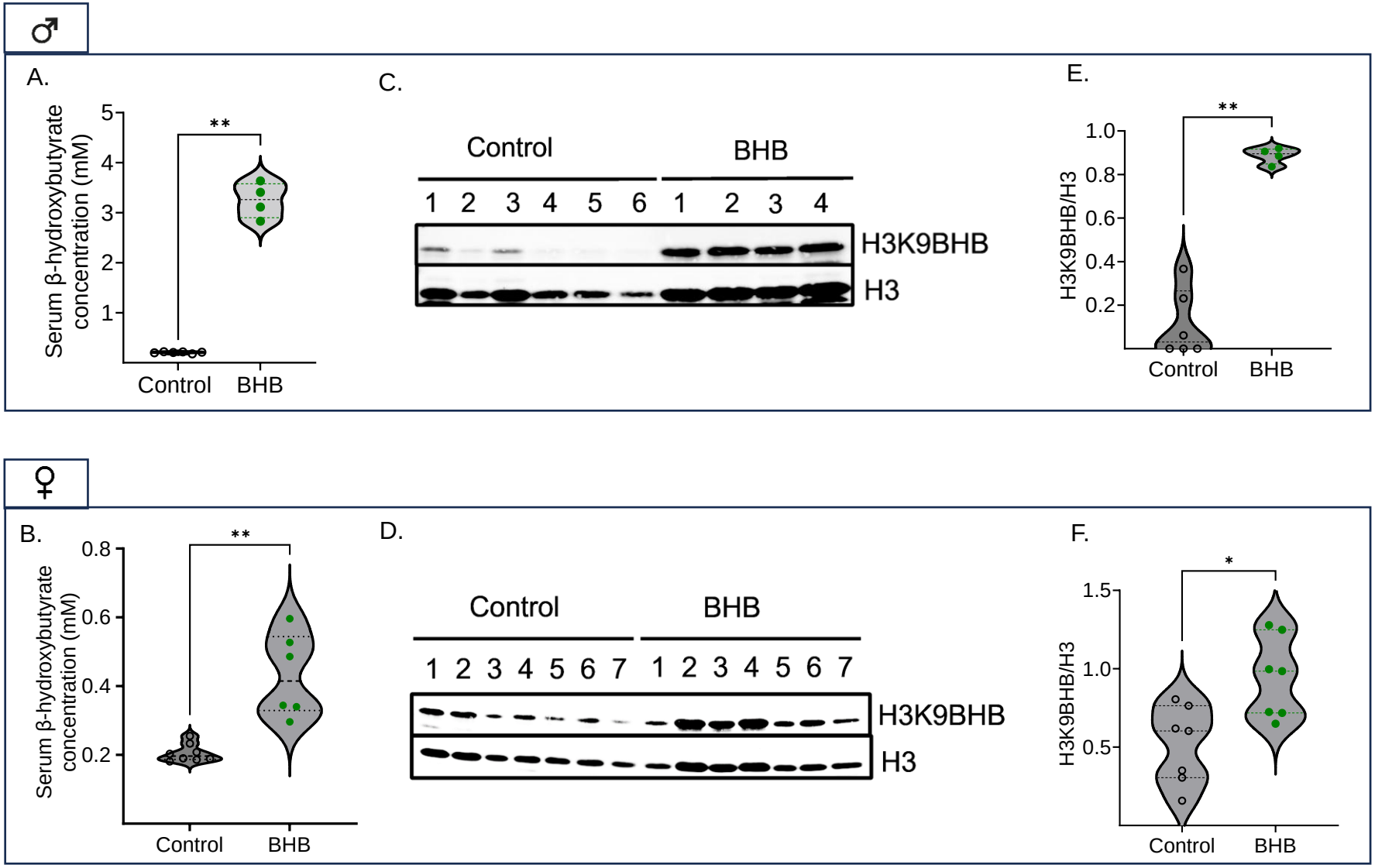
♂
A.
Serum β-hydroxybutyrate concentration (mM)
5
4
3
2
1
**
Control
BHB
C.
Control
BHB
1 2 3 4 5 6 1 2 3 4
H3K9BHB
H3
E.
H3K9BHB/H3
1.0
0.8
0.6
0.4
0.2
**
Control
BHB
♀
B.
Serum β-hydroxybutyrate concentration (mM)
0.8
0.6
0.4
0.2
**
Control
BHB
D.
Control
BHB
1 2 3 4 5 6 7 1 2 3 4 5 6 7
H3K9BHB
H3
F.
H3K9BHB/H3
1.5
1.0
0.5
*
Control
BHB

Figure 3

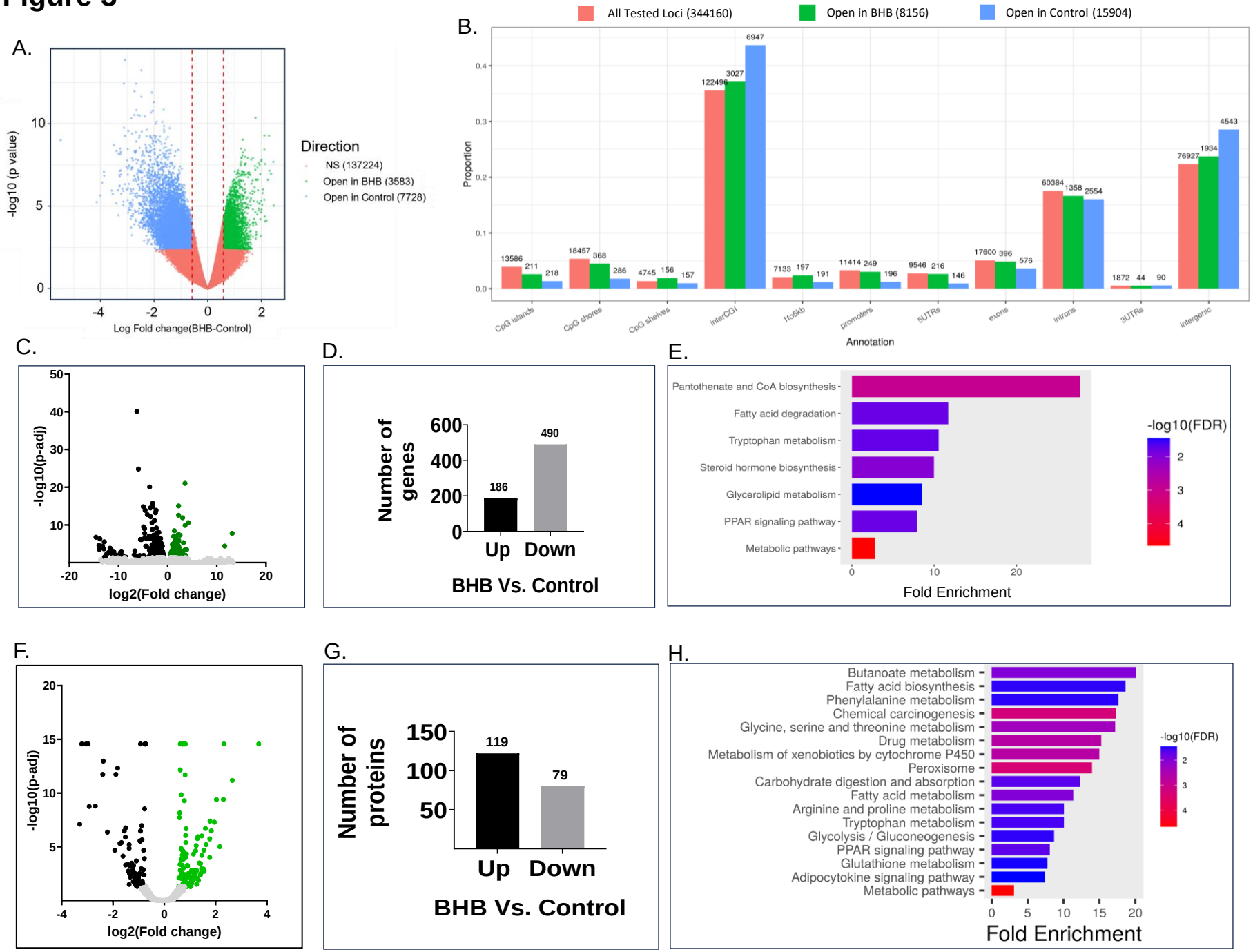
A.
-log10 (p value)
Log Fold change(BHB-Control)
Direction
NS (137224)
Open in BHB (3583)
Open in Control (7728)
B.
All Tested Loci (344160)
Open in BHB (8156)
Open in Control (15904)
Proportion
CpG islands
CpG shores
CpG shelves
InterCGI
1to5kb
promoters
5UTRs
exons
introns
3UTRs
intergenic
Annotation
C.
-log10(p-adj)
log2(Fold change)
D.
Number of genes
186
490
Up
Down
BHB Vs. Control
E.
Pantothenate and CoA biosynthesis
Fatty acid degradation
Tryptophan metabolism
Steroid hormone biosynthesis
Glycerolipid metabolism
PPAR signaling pathway
Metabolic pathways
-log10(FDR)
Fold Enrichment
F.
-log10(p-adj)
log2(Fold change)
G.
Number of proteins
119
79
Up
Down
BHB Vs. Control
H.
Butanoate metabolism
Fatty acid biosynthesis
Phenylalanine metabolism
Chemical carcinogenesis
Glycine, serine and threonine metabolism
Drug metabolism
Metabolism of xenobiotics by cytochrome P450
Peroxisome
Carbohydrate digestion and absorption
Fatty acid metabolism
Arginine and proline metabolism
Tryptophan metabolism
Glycolysis / Gluconeogenesis
PPAR signaling pathway
Glutathione metabolism
Adipocytokine signaling pathway
Metabolic pathways
-log10(FDR)
Fold Enrichment

Figure 3

I.

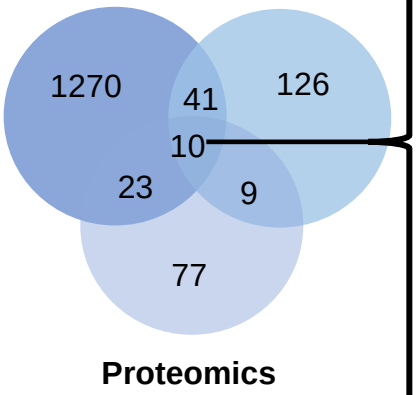

Upregulated genes

Hmgcs2	3-hydroxy-3-methylglutaryl-Coenzyme A synthase 2
Acaa1b	Acetyl-Coenzyme A acetyltransferase 1B
Cyp2d4	Cytochrome P450, family 2, subfamily d, polypeptide 4
Cyp2e1	Cytochrome P450, family 2, subfamily e, polypeptide 1
Slco2a1	Solute carrier organic anion transporter family, 2a1
Slc5a10	Solute carrier family 5 member 10
Arg2	Arginase 2
Bhmt	Betaine-homocysteine S-methyltransferase
Prodh1	Proline dehydrogenase 1
Vnn1	Vanin-1

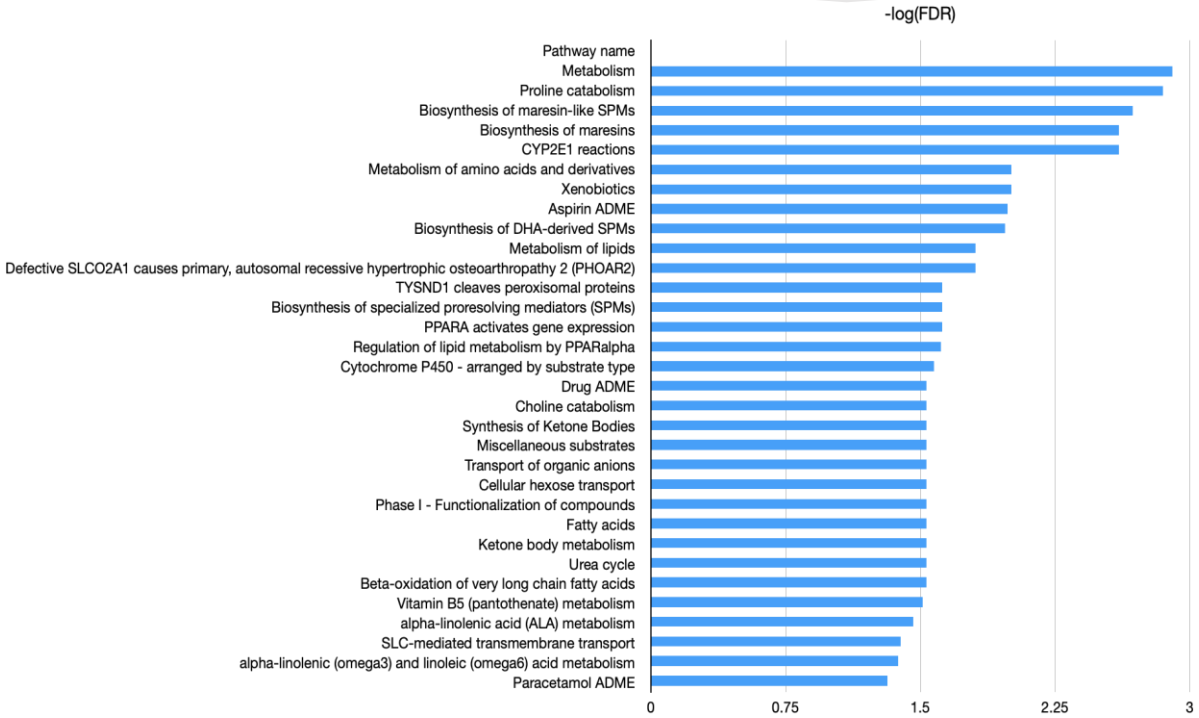

J.

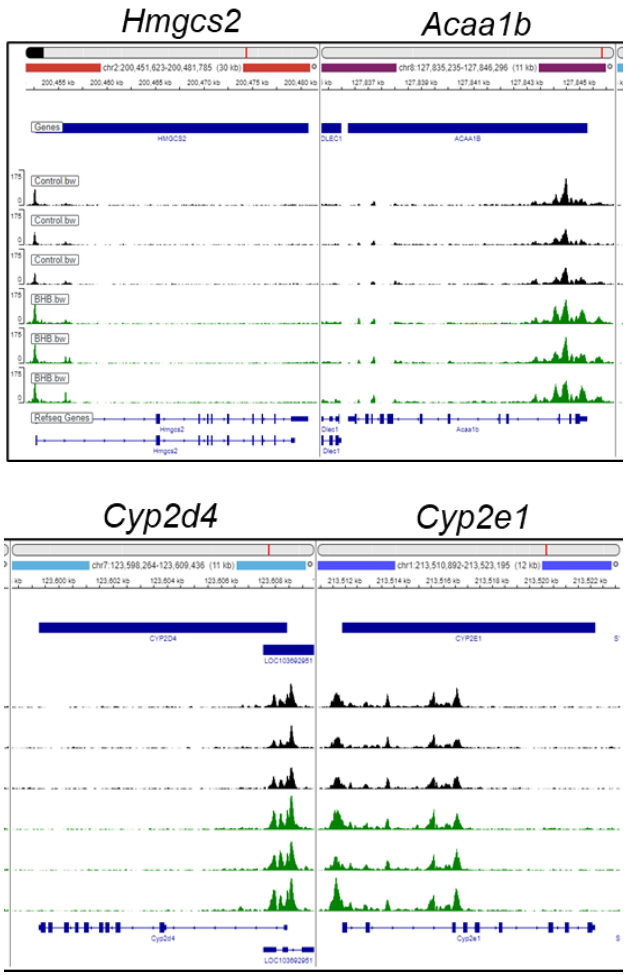

Figure 4

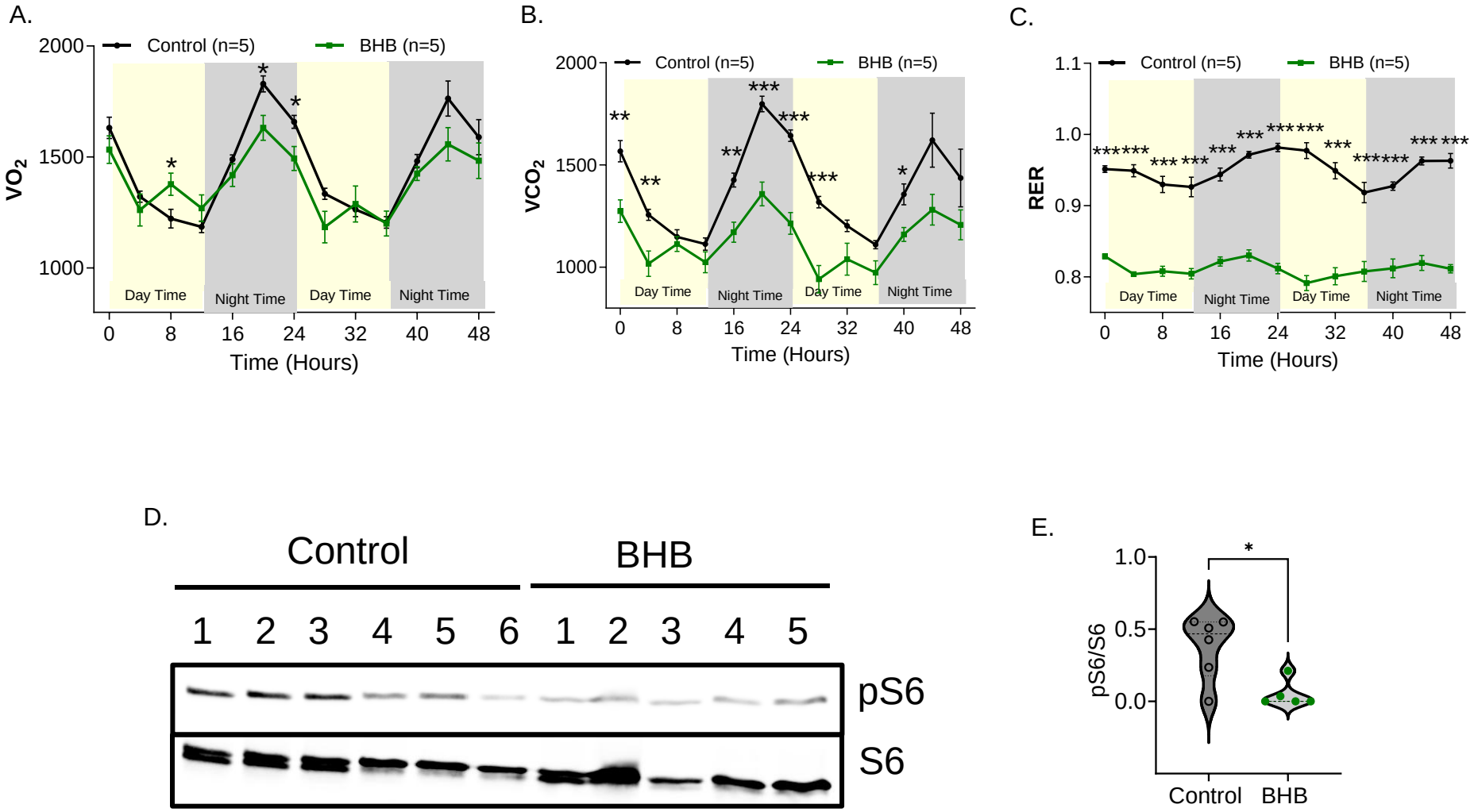
A.
Control (n=5)
BHB (n=5)
VO2
2000
1500
1000
Day Time
Night Time
Day Time
Night Time
0
8
16
24
32
40
48
Time (Hours)
B.
Control (n=5)
BHB (n=5)
VCO2
2000
1500
1000
Day Time
Night Time
Day Time
Night Time
Time (Hours)
C.
Control (n=5)
BHB (n=5)
RER
1.1
1.0
0.9
0.8
Day Time
Night Time
Day Time
Night Time
Time (Hours)
D.
Control
BHB
1 2 3 4 5 6 1 2 3 4 5
pS6
S6
E.
pS6/S6
1.0
0.5
0.0
Control
BHB

Figure 5

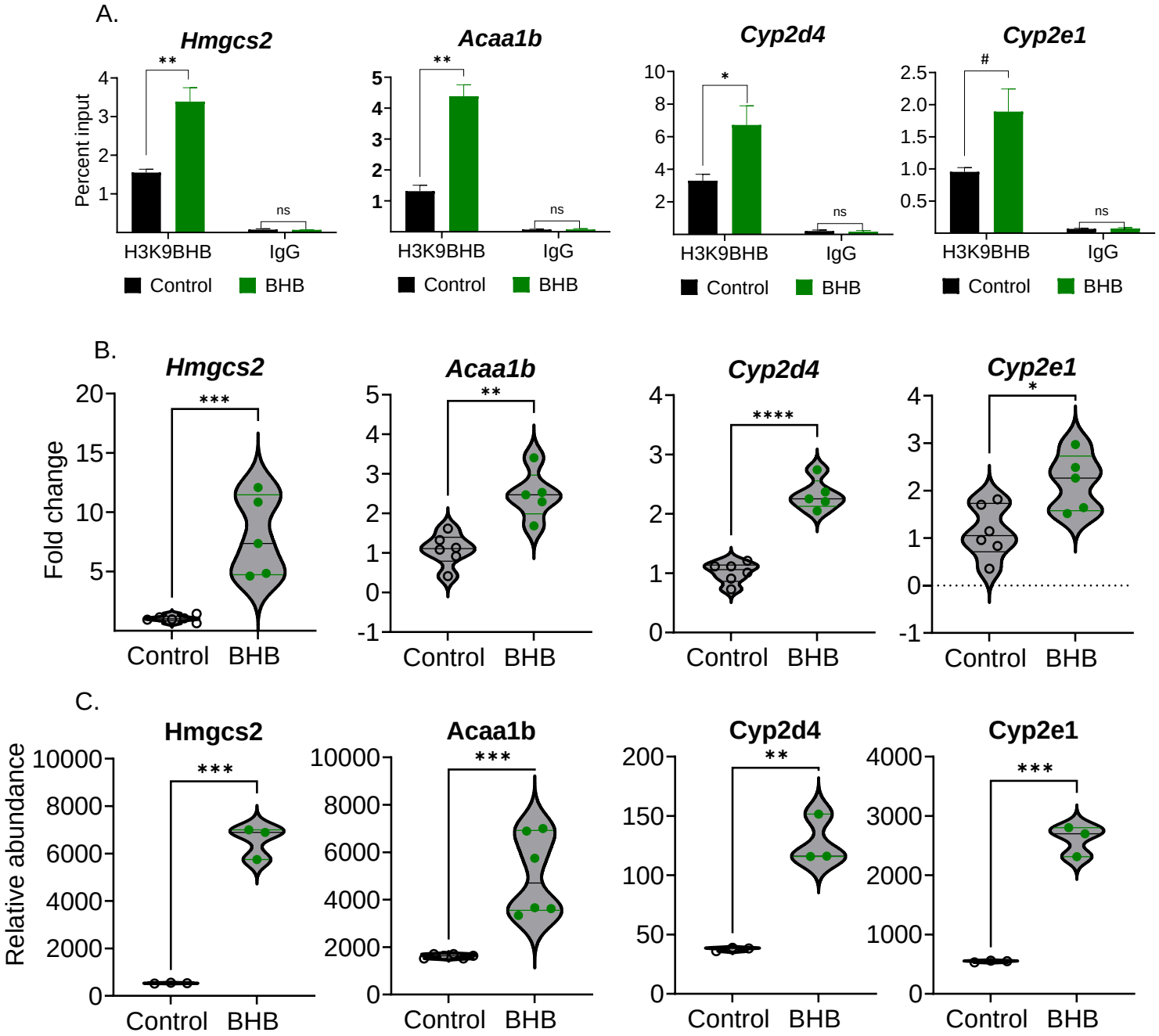
A.
Hmgcs2
Acaa1b
Cyp2d4
Cyp2e1
Percent input
H3K9BHB
IgG
Control
BHB
ns
B.
Fold change
C.
Relative abundance

Figure 6

A.

Control

BHB

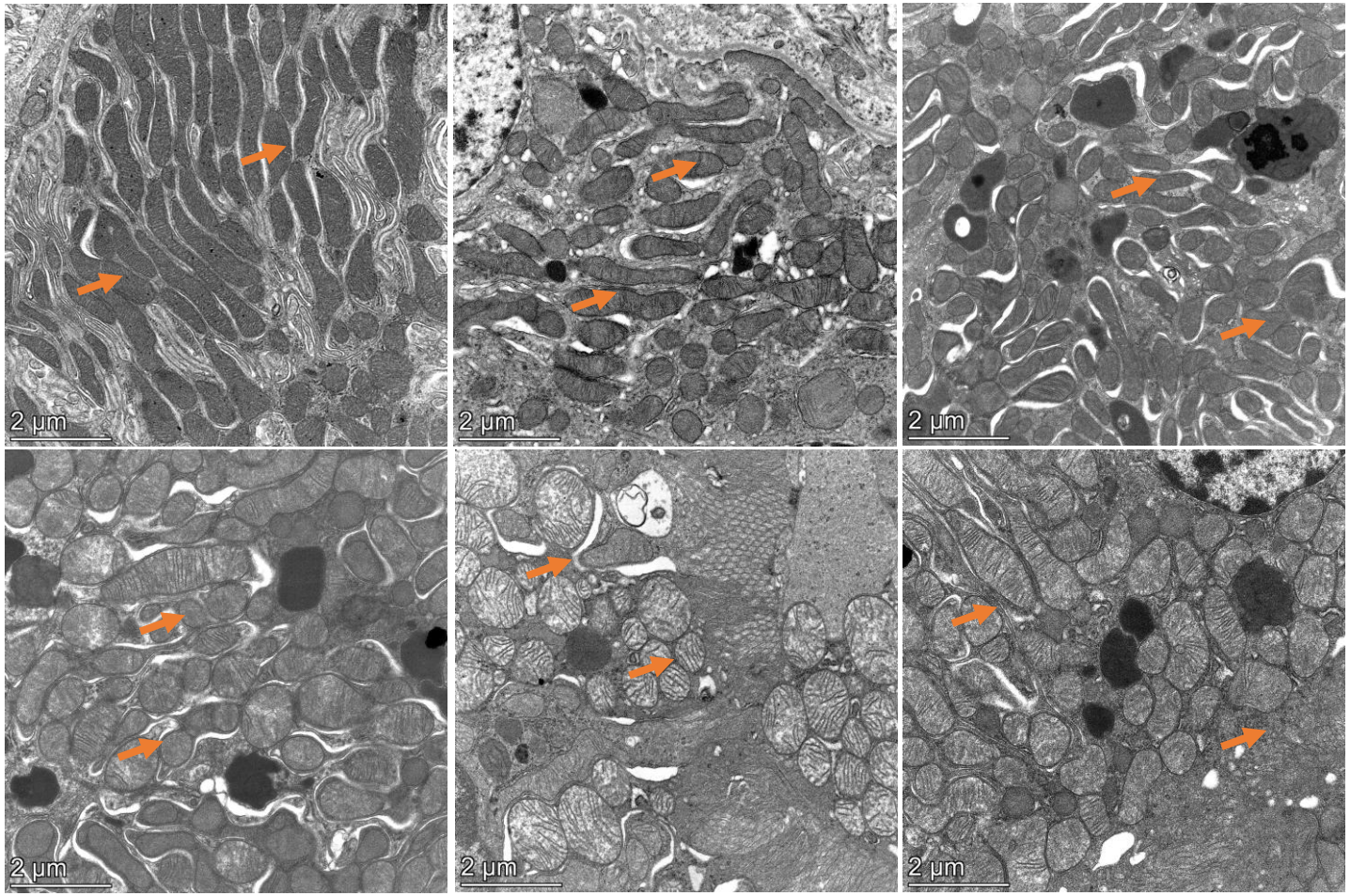

B.

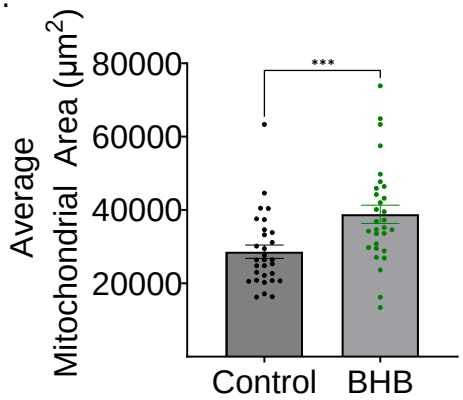

C.

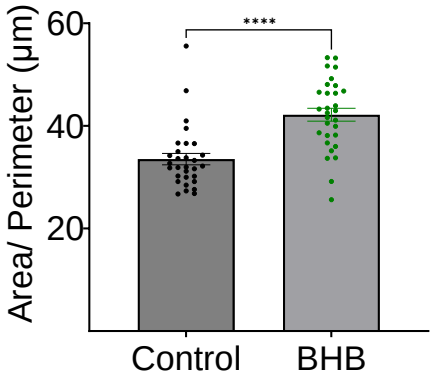

D.

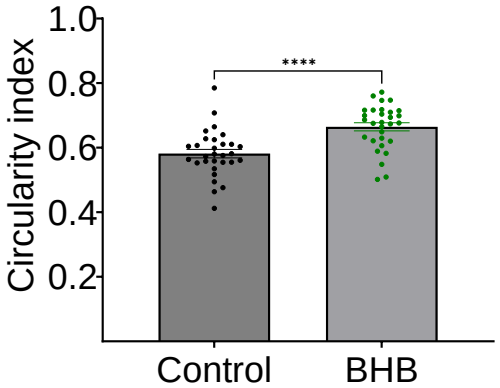

Figure 7

A.

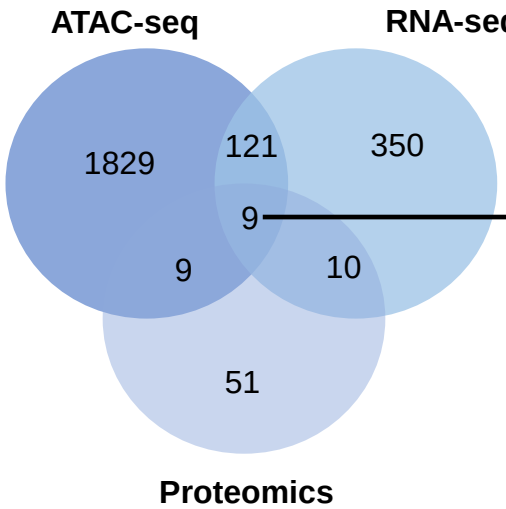

Downregulated genes

Ptprc	Protein Tyrosine Phosphatase Receptor Type C
Lcp1	Lymphocyte Cytosolic Protein 1
Lama1	Laminin Subunit Alpha 1
Pld4	Phospholipase D Family Member 4
Ptn	Pleiotrophin
Akr1c15	Aldo-Keto Reductase Family 1 Member C15
RT1-Ba	Major Histocompatibility Complex, Class II, DQ Alpha 1
RT1-Da	Major Histocompatibility Complex, Class II, DR Alpha
Rac2	Rac Family Small GTPase 2

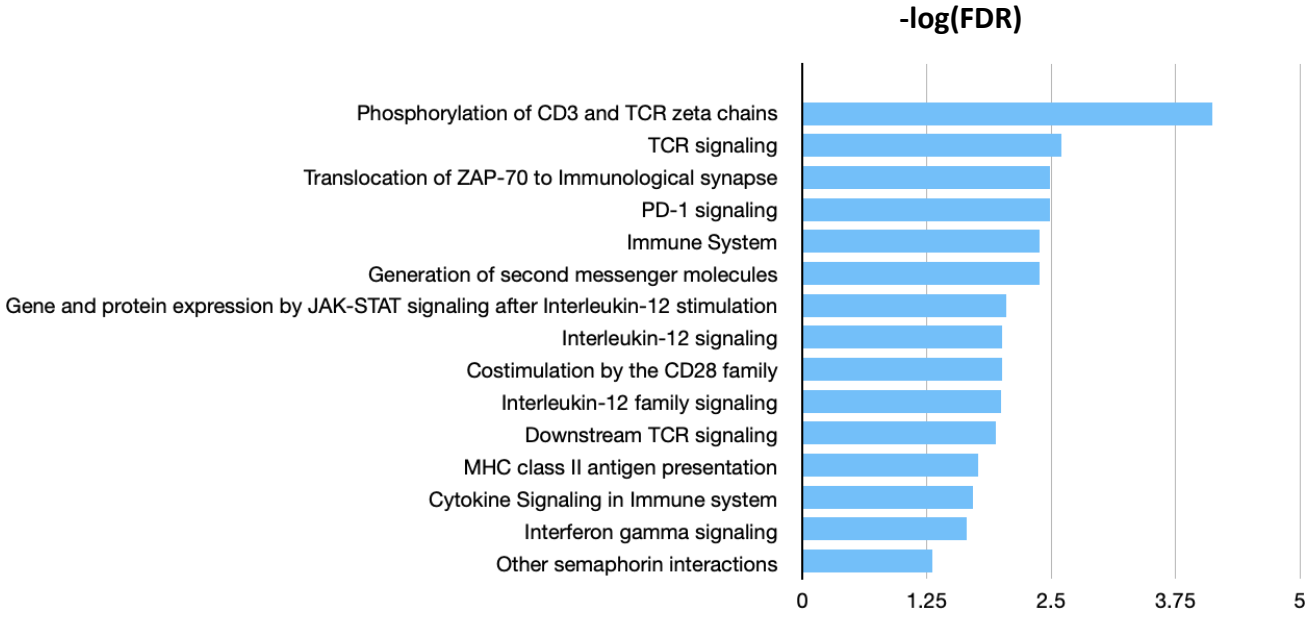

B.

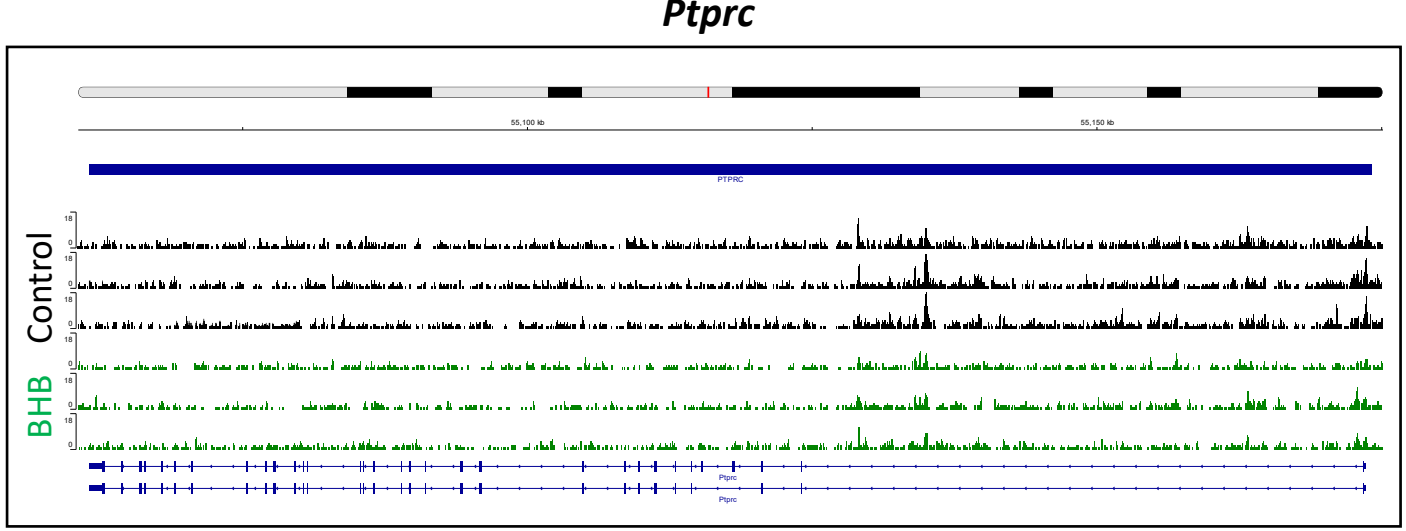
Ptprc
55,100 kb
55,150 kb
PTPRC
Control
BHB
Ptprc
Ptprc

C.

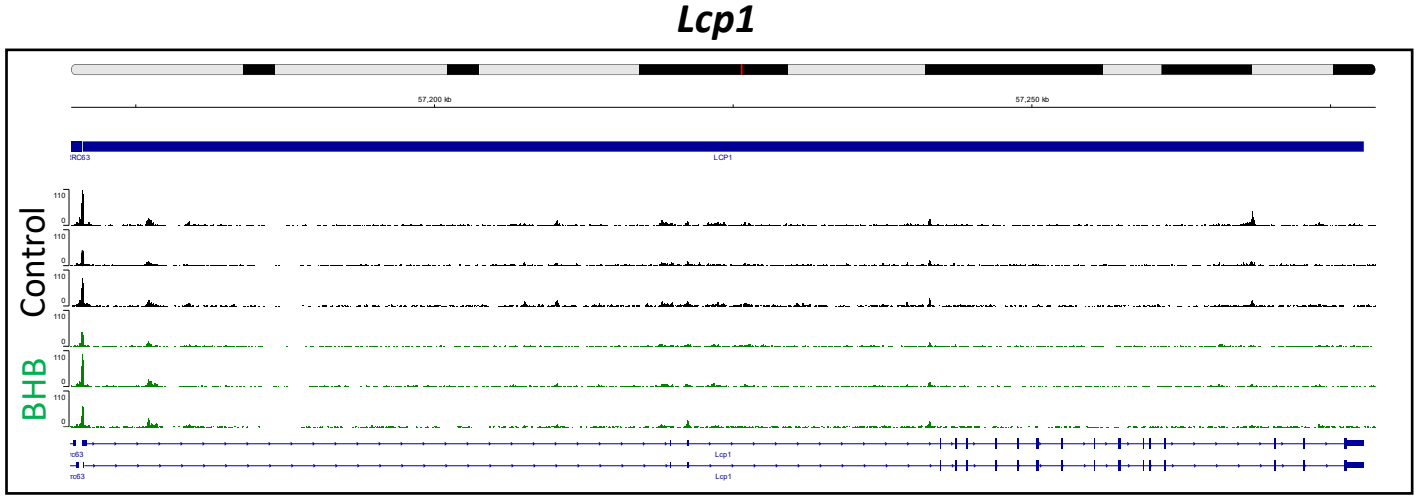
Lcp1
57,200 kb
57,250 kb
LCP1
Control
BHB
Lcp1
Lcp1

D.

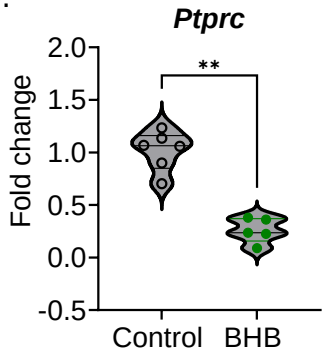
Ptprc
**
Fold change
2.0
1.5
1.0
0.5
0.0
-0.5
Control
BHB

E.

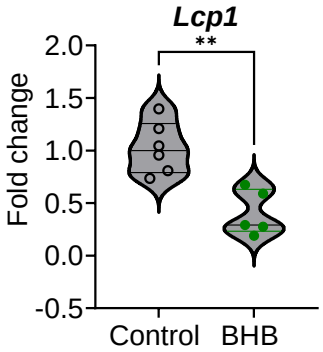
Lcp1
**
Fold change
2.0
1.5
1.0
0.5
0.0
-0.5
Control
BHB

F.

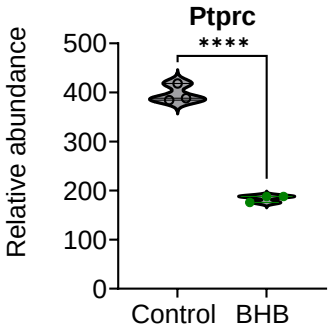
Ptprc
****
Relative abundance
500
400
300
200
100
0
Control
BHB

G.

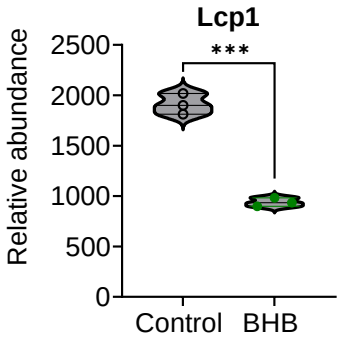
Lcp1
***
Relative abundance
2500
2000
1500
1000
500
0
Control
BHB

H.

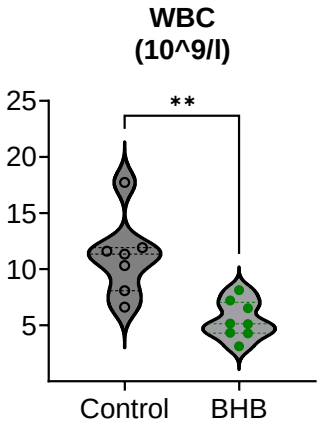

I.

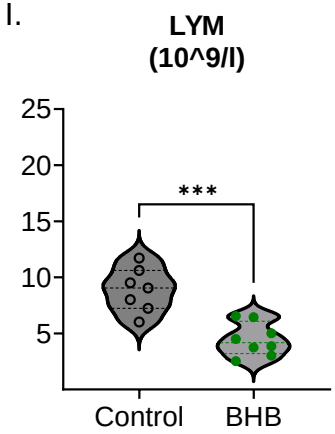

K.

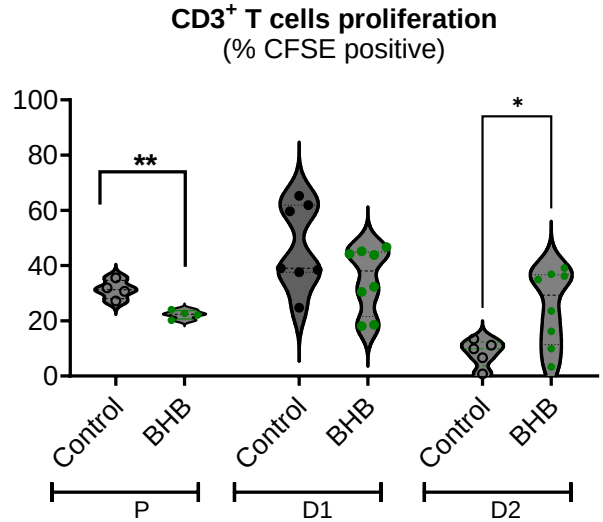

J.

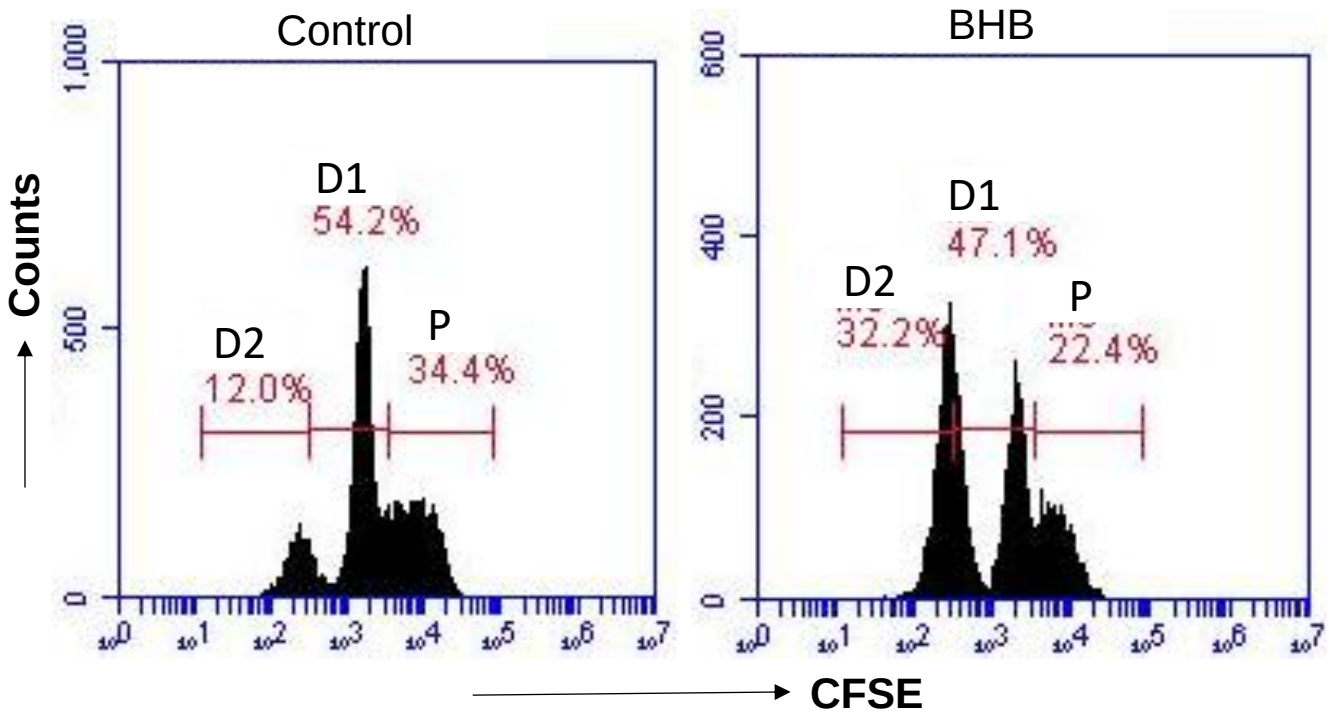

P= Parent population
D1= Daughter 1
D2= Daughter 2

Supplementary Figure 1

A.

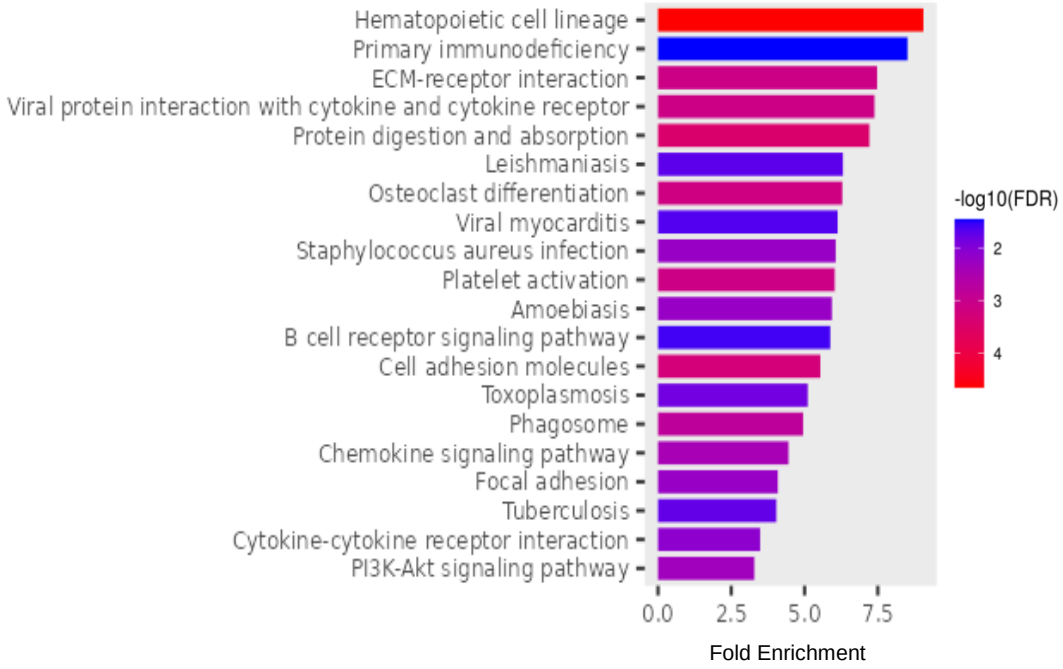

B.

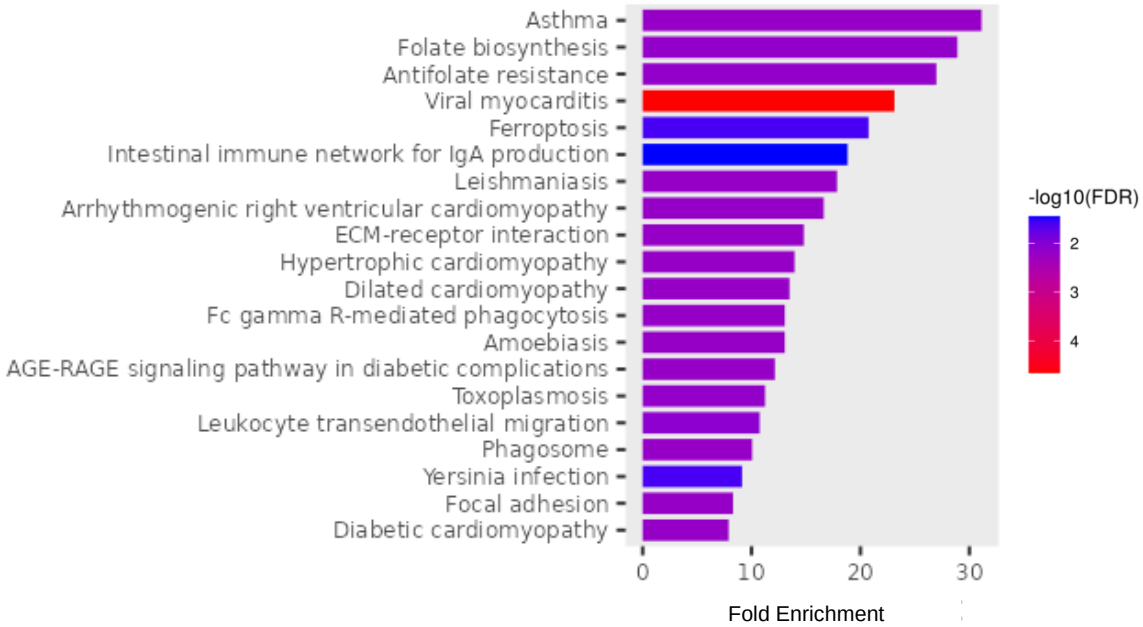

Supplementary Figure 2

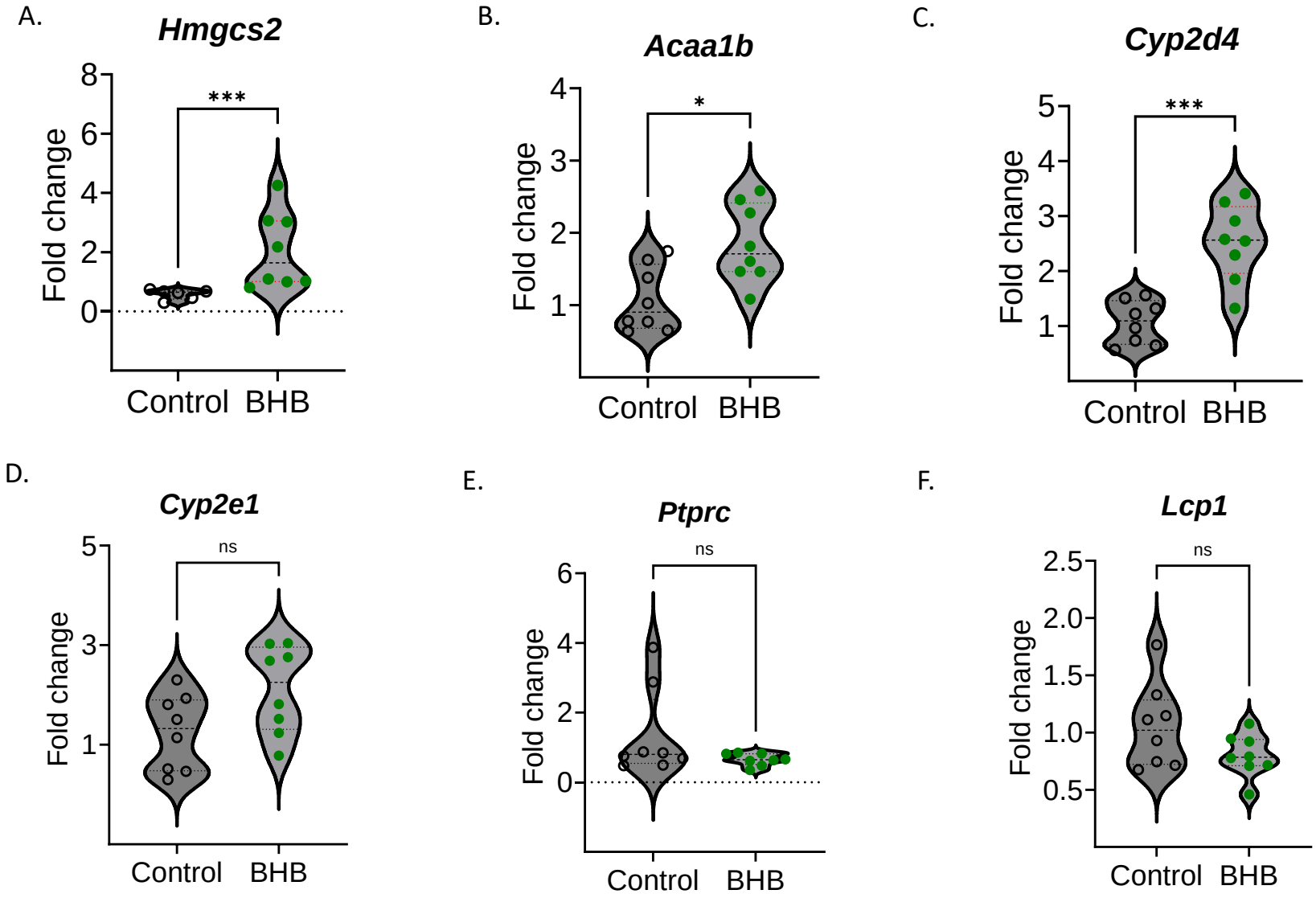

Supplementary Figure 3

A.

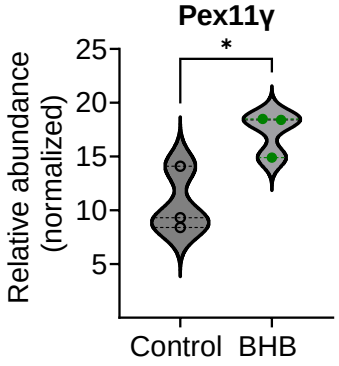

B. Control (IHC-Pmp70)

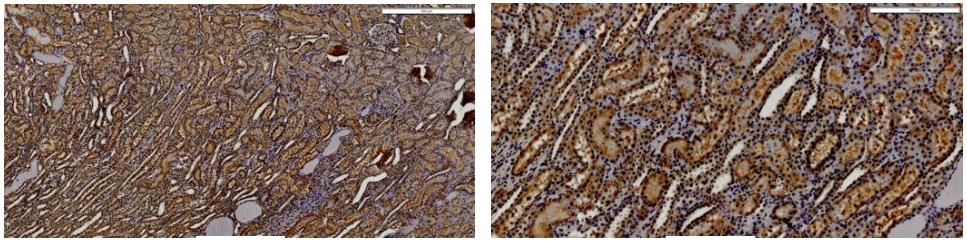

8x 40x

C. BHB (IHC-PMP70)

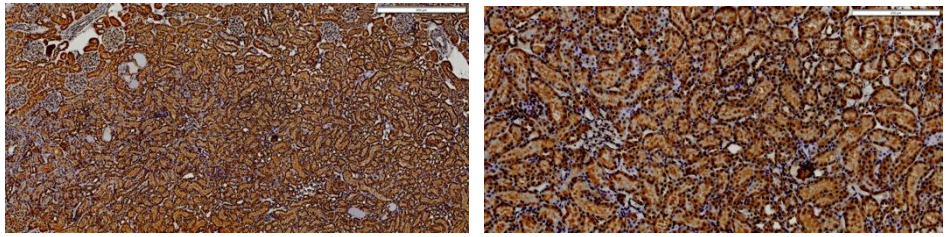

8x 40x

Supplementary Figure 4

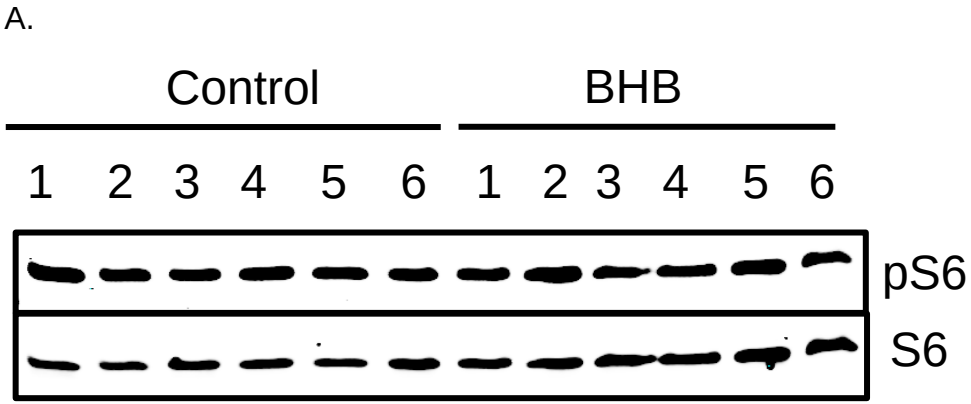

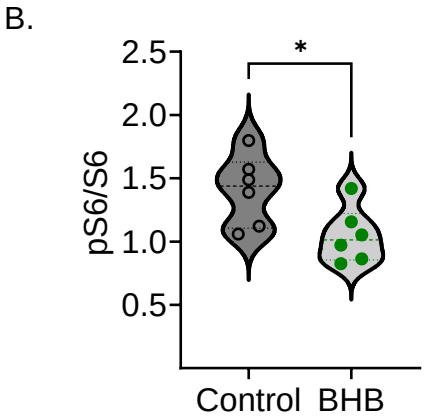

Supplementary Figure 5

A.

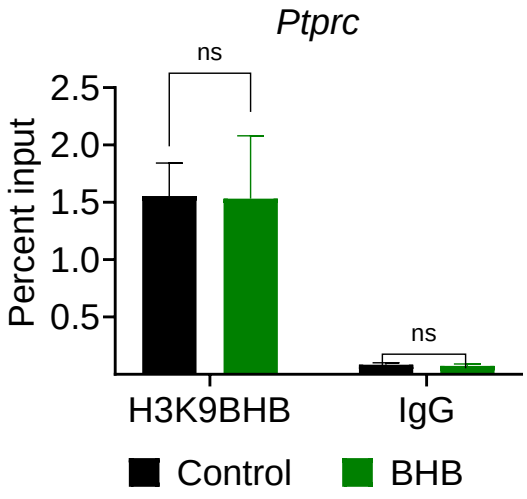

B.

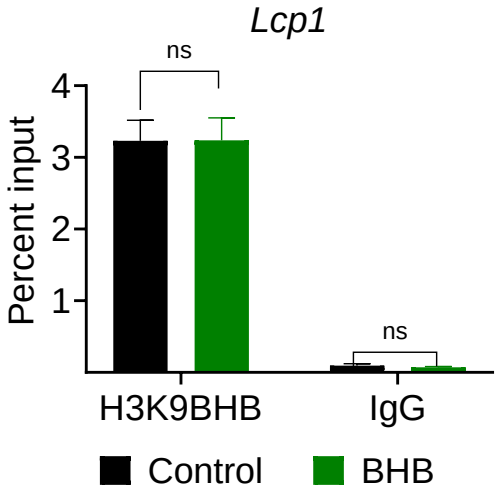

C.

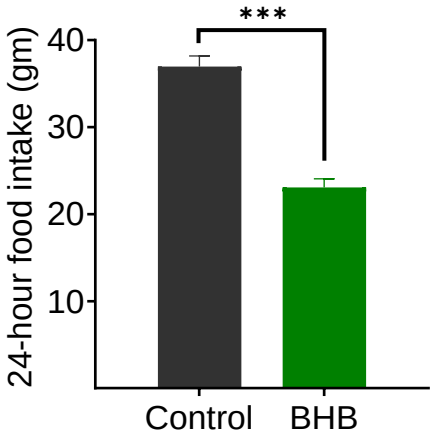

D.

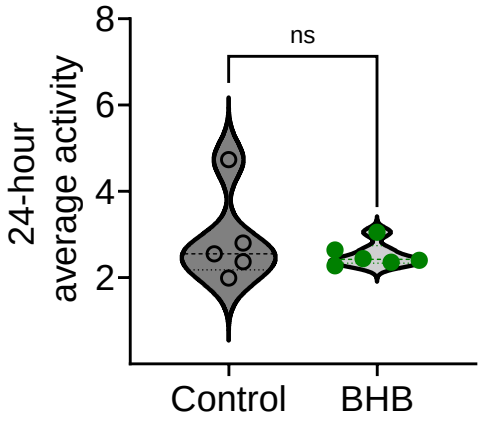
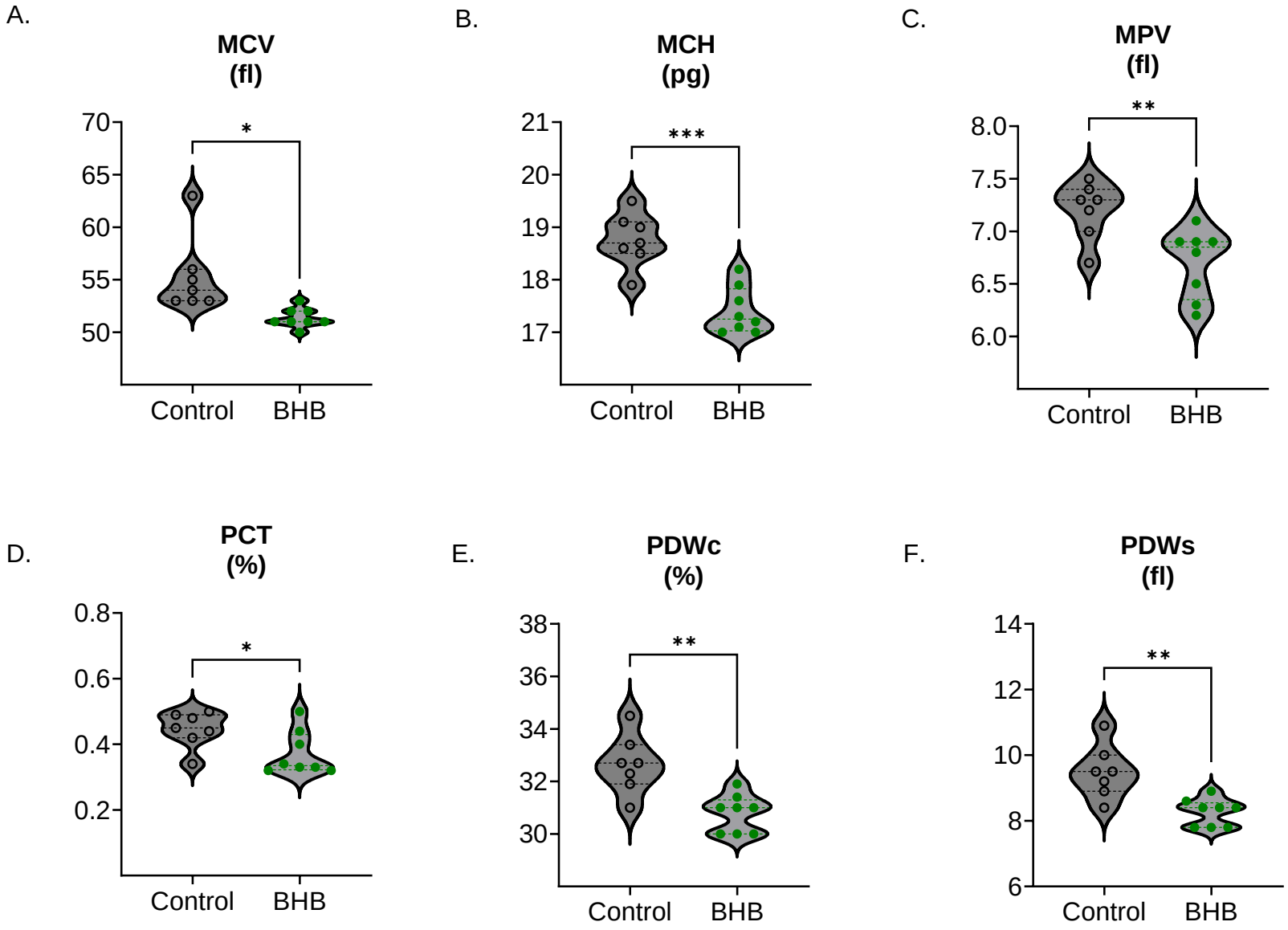
Supplementary Figure 6